DEVELOPING PROXIES FOR LATE HOLOCENE SEA-LEVEL AND CLIMATE CHANGE ALONG THE NORTHEASTERN GULF OF MEXICO COAST

By

TYLER MCNABB

Bachelor of Science in Geology

Florida Atlantic University

Boca Raton, Florida

2012

Submitted to the Faculty of the
Graduate College of the
Oklahoma State University
in partial fulfillment of
the requirements for
the Degree of
MASTER OF SCIENCE
December, 2014

DEVELOPING PROXIES FOR LATE HOLOCENE

SEA-LEVEL AND CLIMATE CHANGE ALONG

THE NORTHEASTERN GULF OF MEXICO COAST

Thesis Approved:

Dr. Joseph F. Donoghue

Thesis Adviser

Dr. Eliot Atekwana

Dr. Todd Halihan

Name: TYLER MCNABB

Date of Degree: DECEMBER, 2014

Title of Study: DEVELOPING PROXIES FOR LATE HOLOCENE SEA-LEVEL AND CLIMATE CHANGE ALONG THE NORTHEASTERN GULF OF MEXICO COAST

Major Field: GEOLOGY

Abstract: The goal of this investigation was to develop sea-level and climate proxies for the northeastern Gulf of Mexico during the late Holocene. The purpose was to help better understand the relationship between climate change and fluctuations in sea-level and storm frequency. The data sources were a ground-penetrating radar (GPR) transect across a barrier island beach ridge plain on the northwestern coast of Florida, and a sediment core from a coastal lake on the same barrier island. The study site was St. Vincent Island, a barrier island beach ridge plain. The GPR data have been used to develop a proxy for sea-level change, while the sediment core has been analyzed for proxy evidence of paleo-storm occurrence. The process by which the study was conducted was as follows: 1) determine sedimentation rates and sediment characteristics in a coastal sediment core using radiocarbon, lead-210 dating, and a new method with a laser particle analyzer; 2) use the chronology of known historic hurricanes to determine the signature of major storms in the historic portion of the sediment record; 3) employ the storm signature to create a paleo-storm proxy in the long-term sediment record; 4) process and utilize a new method to analyze field GPR data to determine past sea-levels, based on the depth of basal deposits of the ridges in a beach ridge succession; and 5) correlate the sea-level history and paleo-storm occurrences to the regional climate history based on published proxy studies. Both climate-related proxies were found to correlate with previous proxies developed for this region. The new method of determining paleo-sea level, through use of the GPR data, was successful at determining paleo-sea level.

TABLE OF CONTENTS

Chapter Page

LIST OF TABLES

Table Page

LIST OF FIGURES

Figure Page

Figure Page

Figure Page

CHAPTER I

INTRODUCTION

This chapter explains the objectives of this study. The history of late Holocene sea-level and climate change is examined, along with a description of the study area. In addition, previous proxies recording late Holocene climate change will be discussed, as well as the hypotheses that were tested in this study.

1.1 Objective

With sea-surface temperatures (SSTs) rising, and hurricane intensity in the Atlantic increasing since over the past half century, understanding the long-term history of major storms and how they are affected by climate change becomes increasingly more important. Recent global climate models predict the frequency of intense hurricane activity (category 4 and 5 storms) will double by the end of the 21st century (Elsner et al., 2008; Bender et al., 2010; Knutson et al., 2010). The goal of this investigation was to develop sea-level and climate proxies for the northeastern Gulf of Mexico during the late Holocene. The proxy data consist of a ground-penetrating radar (GPR) transect across a barrier island beach ridge plain, and a sediment core from a coastal lake on the same island. The GPR data were collected on St. Vincent Island, on the coast of northwest Florida near Apalachicola. The core used for the sediment analysis was

collected in Oyster Pond, a coastal pond on the seaward side of the island. The GPR data was used to develop a proxy for sea-level change, while the sediment core was analyzed for proxy evidence of paleo-storm occurrence. The objectives of the study were: 1) determine sedimentation rates and sediment characteristics in a coastal sediment core using age constraints and sediment grain characterisitcs; 2) use the chronology of known historic hurricanes to determine the signature of major storms in the historic sediment record; 3) employ the storm signature to create a paleo-storm proxy in the long-term sediment record; 4) process and analyze field GPR data to determine past sea-levels, based on the depth of basal deposits of the ridges in a beach ridge succession; and 5) correlate the sea-level history and paleo-storm occurrences to the regional climate history based on published proxy studies. The two climate-related proxies were found to correlate with previous proxies developed for this region, as reported in the published literature. In addition, by creating a sea-level proxy based on GPR data, a new method of determining paleo-sea level was developed, along with development of a quicker and higher-resolution method for determining paleo-storm frequency by using sediment grain characteristics.

1.2 Late Holocene Sea Level and Climate Change

Global sea level has been fluctuating but generally rising throughout the Holocene (Fairbridge, 1961; Shepard, 1963, 1964). Multiple sea-level curves covering the Holocene have been created using a variety of proxies, including sedimentologic studies, geochemical studies, and/or studies involving shoreline indicators. In addition to relating sea-level changes to climate, paleo-storm occurrence also has been proposed to correlate with climate change (Kerr, 2001; Forrest, 2007; Elsner et al., 2008; McCarthy, 2009, Coor, 2012). While developing proxy records of past storm occurrences at a particular location, it is important to assess whether observed variability of hurricane occurrences is related to changing climate or simply due to a random

clustering of events during a constant climate (Woodruff et al., 2008). Better understanding previous hurricane activity is an ongoing process. Although a record of hurricane activities is available for North America only as far back as 130 years, this record reveals variability in hurricane activity, which can be related to climatic events such as El Niño/Southern Oscillation (ENSO) events (Liu and Fearn, 2000).

Models have shown that sea-level change correlates with climate change (Grinsted and Jevrejeva, 2009). The Last Glacial Maximum (approximately 18,000 years ago) reached a lowstand of approximately -120 m, and between 5,000 and 7,000 years ago sea level reached near modern levels (Balsillie and Donoghue, 2004; Donoghue, 2011; Fairbanks, 1989; Forrest, 2007). Sea-level lowstands have been determined in northern Gulf of Mexico proxy records at 4000 years BP, 2400 years BP, 1100 years BP, and between 600 and 400 years BP (Balsillie and Donoghue, 2004; Garrison et al., 2010; Stapor and Stone, 2004; Tanner, 1991, 1992).

Globally, current temperatures have not reached peak interglacial values. However, these current temperatures (a temperature anomaly of approximately 0.6°C) are warmer than roughly 75% of Holocene history (Marcott et al., 2013). In addition to these warmer temperatures, climate model projections for the twenty-first century indicate that warming tropical sea-surface temperature (SST) makes the tropical environment more favorable to tropical cyclones (Vecchi and Knutson, 2008).

It is important to note that microtidal barrier islands in the Gulf of Mexico record evidence of sea level cycles of 400 to 500 years during the late Holocene (Garrison et al., 2010). Although many sea-level and paleo-storm proxies have been developed, sea level fluctuations in the late Holocene remains a topic of debate (Coor, 2012). Therefore, additional proxies can aid in a better understanding of recent climate change and its effect on sea level and intense storm frequency.

1.3 Study Area

St. Vincent Island is located on the Northwest coast of Florida, approximately in the middle of the Florida panhandle coast (Fig. 1). Several seasonal freshwater coastal dune lakes have developed along the island coastline (Foster, 2000). This barrier island is 14 km long and 6 km wide on its east end, and is one of the largest barrier islands in the Gulf coast. (Forrest, 2007). The island is approximately 4,000 years in age and has built out into the Gulf of Mexico as an extensive beach-ridge plain with over 100 beach ridges (Fig. 2) (Forrest, 2007). These ridges have been divided into 12 different sets (Forrest, 2007). The oldest of these ridge sets are located on the northernmost side. The beach-ridge sets become progressively younger from north to south (Fig. 3). The older beach ridges are generally lower in elevation than the younger beach ridges, and all of them are concave seaward (Forrest, 2007). Coastal sediment transport in this region is dominated by net longshore transport from east to west, as evidenced by the westward tapering of the beach-ridge sets (Stapor, 1975; Stone et al., 1996). The island is relatively stable with respect to sea-level rise, although in several places the shoreline is eroding due to the island's orientation toward the direction of the most energetic storm waves (Stone and Penland, 1992).

Oyster Pond (Fig. 4) is located on St. Vincent Island, and is a freshwater pond that lies approximately 0.35 km from the Gulf of Mexico (Coor, 2012). The pond is separated from the Gulf by younger beach ridges within the same ridge set to the south and west. The pond surface has an elevation of 0.25 meters above sea level, with a small slough exiting it (Coor 2012). This slough historically has only been opened up by major storms, and during recent time has been dammed by natural processes (Coor 2012).

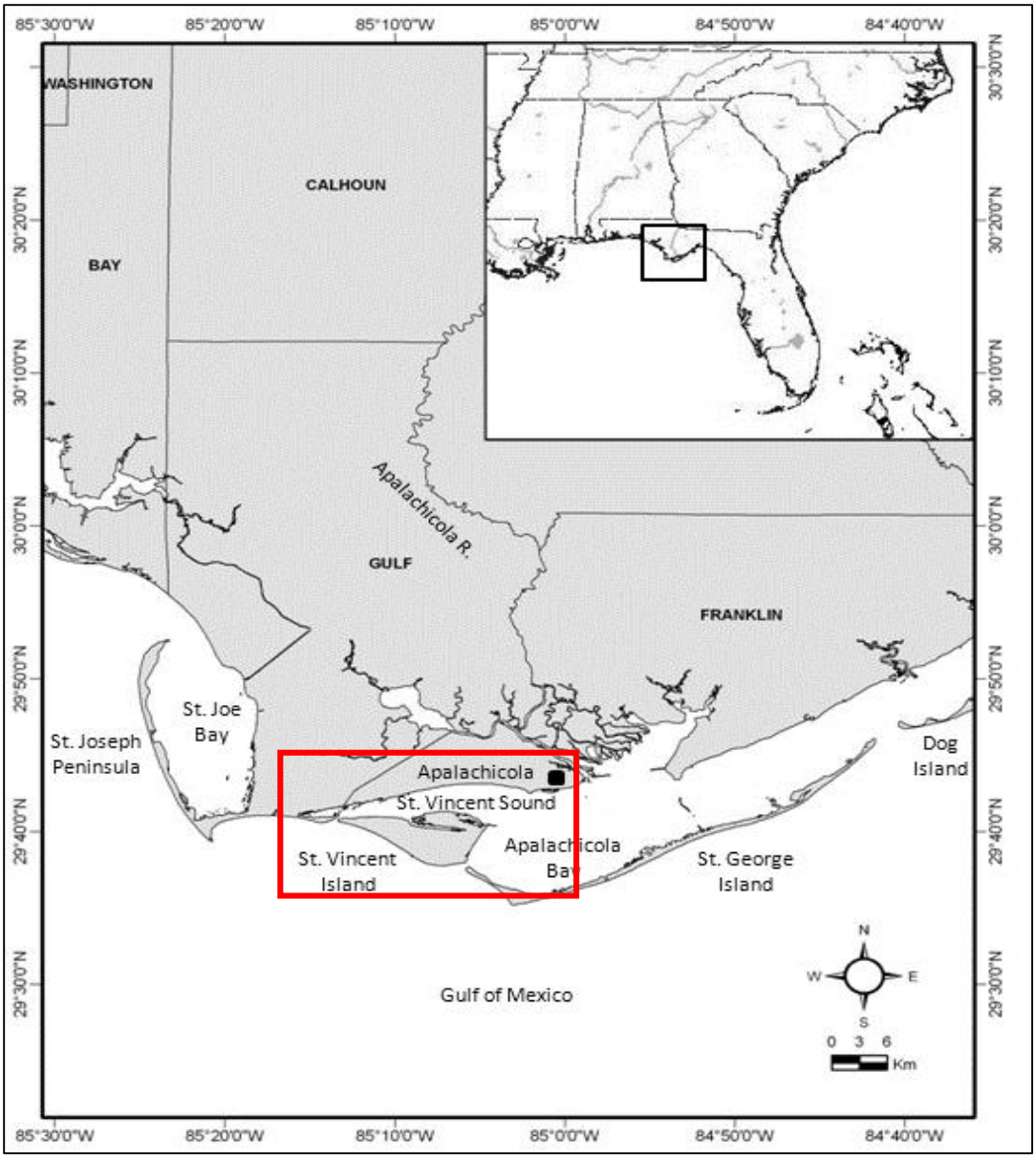

Fig. 1. Location map of St. Vincent Island study area (red rectangle), on the northwest Florida coast (Forrest, 2007).

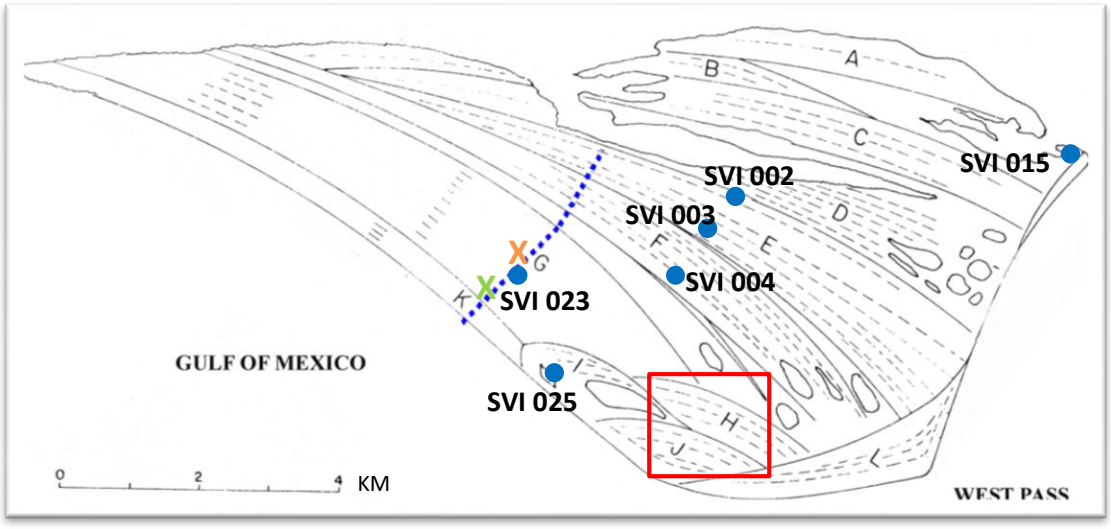

Fig. 2. St. Vincent Island, study area as well as ridge sets (letters A-L) comprising the island's beach ridge plain. Regional location of the island is shown in Fig. 1. The blue dashed line represents Road 4 (where ground-penetrating radar (GPR) transects were taken) in relation to beach ridge sets. The orange X represents the approximate location along Road 4 of the transect segment shown in Fig. 17 (see Results). The green X represents the approximate location along Road 4 of the transect segment shown in Fig. 18 (see Results). The blue filled circles represent the approximate locations of optically-stimulated Optically Stimulated Luminescence (OSL)-dated beach ridges. The red rectangle represents the approximate location of the 3-D light detection and ranging (LIDAR) image shown in Fig. 3 (adapted from Forrest, 2007).

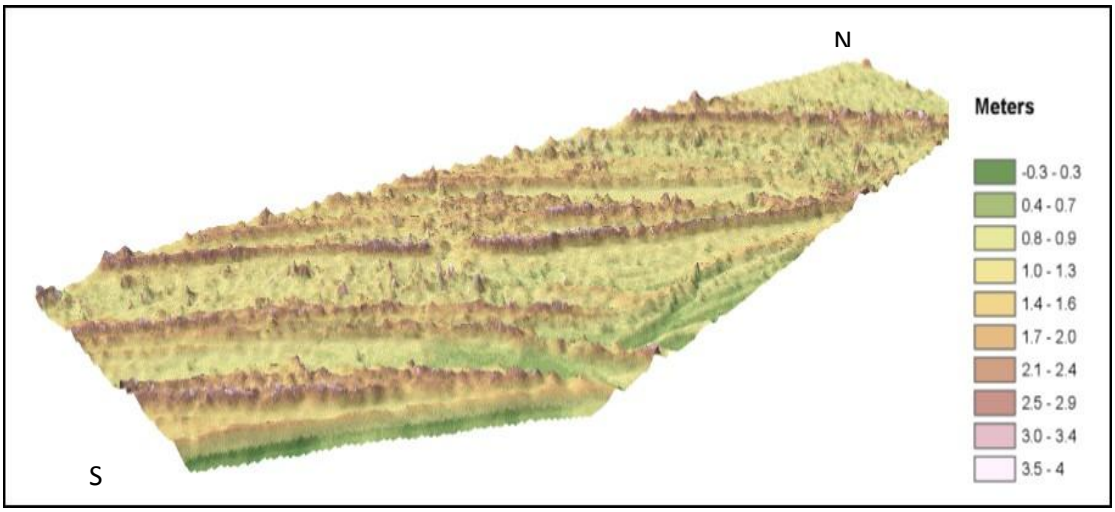

Fig. 3. Example of 3-D light detection and ranging (LIDAR) imagery of the southeastern part of St. Vincent Island showing topographic details of a portion of the extensive beach-ridge plain. Location on St. Vincent Island shown by red rectangle in Fig. 2.

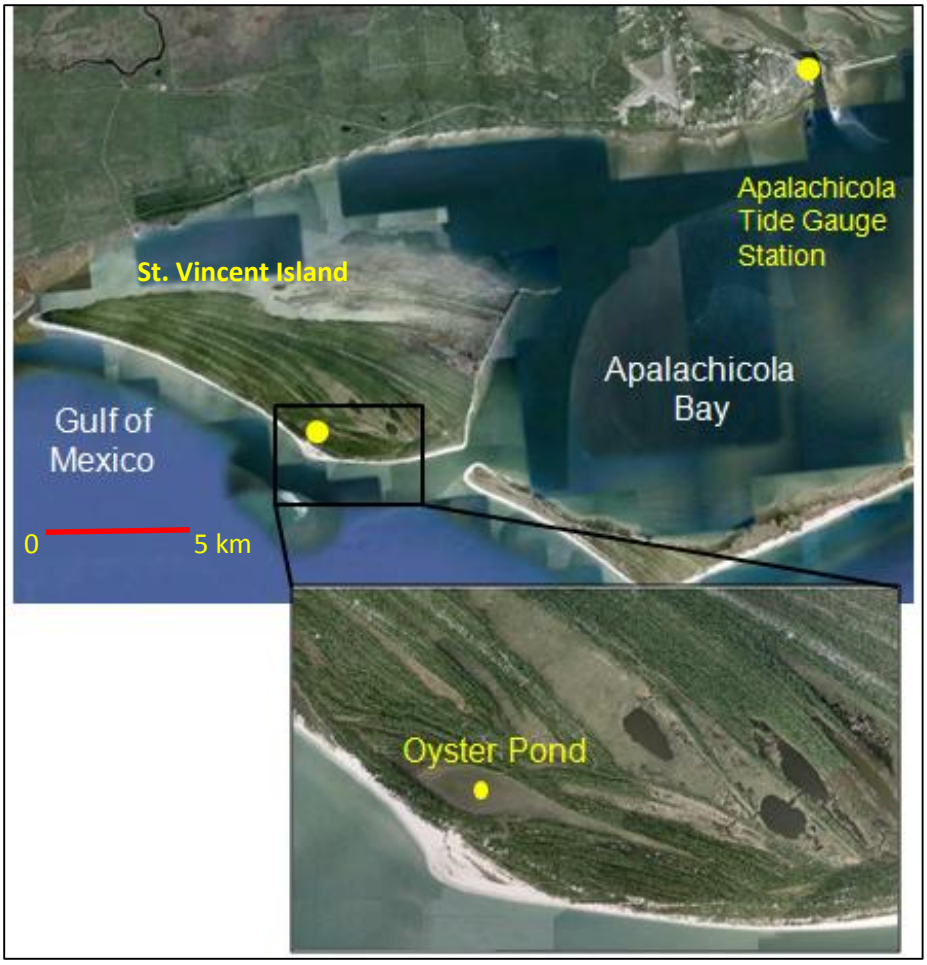

Fig. 4. Satellite images showing location of core 092710-01 collected from Oyster Pond on St. Vincent Island, NW Florida coast, and Apalachicola tide gauge station. Regional location is shown in Fig. 1 (adapted from Coor, 2012).

1.4 Previous Work

In order to employ compare climate proxies, it is important first to address previous studies in the Gulf of Mexico region. By investigating climate proxies for the Gulf of Mexico region, knowledge of late Holocene regional climate change can be gained. The debate regarding the history of Holocene sea level change is not due to a lack of sea-level proxies, but rather due to a lack of reliable data (Forrest, 2007). Reliable sea-level proxies come from sedimentologic studies, geochemical studies, and/or studies involving shoreline indicators, such as beach ridges.

By analyzing these climate proxies, not only can knowledge of the late Holocene climate be gained, but the effect climate has on the geological environment can be better understood. A sampling of climate proxy studies in the region is presented below.

In a regional climate proxy study, a history of hurricane-induced overwash events from Laguna Playa Grande, Vieques, Puerto Rico was developed by Donnelly and Woodruff (2007). Cores were taken from a backbarrier lagoon and sediment analysis was carried out using a laser particle analyzer. Storm-induced deposits were preserved in the sediments taken in the core, and offered a longer time scale for investigating hurricane landfall and the relationship between climate and hurricane activity. In this study by Donnelly and Woodruff (2007), a period of infrequent intense hurricanes was observed between approximately 3600 yr BP and 2600 yr BP (Fig. 5). In the Donnelly and Woodruff (2007) climate proxy, time periods with fewer intense hurricanes were represented by smaller grain size, and time periods with intense hurricane landfalls were depicted by larger grain size. Donnelly and Woodruff (2007) found that the Caribbean experienced times of intense hurricane landfall during periods when the sea-surface temperatures (SST) were on average cooler than modern SST, and that the tropical Atlantic SSTs fluctuated. Additionally Donnelly and Woodruff (2007) observed that the weather phenomena of El Niño/Southern Oscillation (ENSO), influences hurricane activity on centennial and millennial timescale.

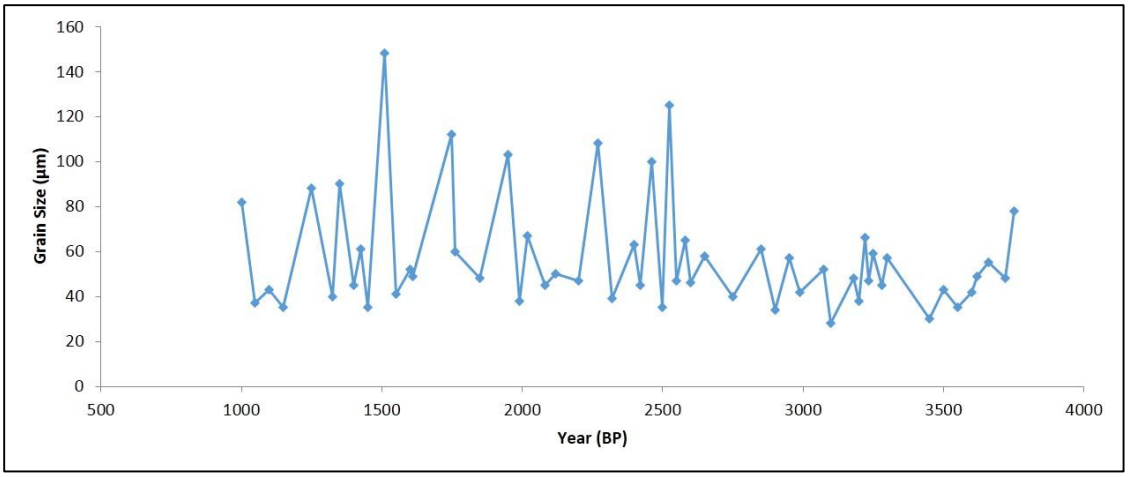

Fig. 5. Mean bulk grain-size record of a core from Laguna Playa Grande, Vieques, Puerto Rico (re-plotted from data in Donnelly and Woodruff, 2007). Variations of grain size are taken to be a proxy indicating changes in the frequency of intense storms. Larger grain size represents times of frequent intense storms, while smaller grain sizes represent times of fewer intense storms.

El Niño/Southern Oscillation (ENSO) has been a topic of intensive study in recent years. It is possible to correlate warm ENSO events to sea surface temperatures (Moy et al., 2002). During warm ENSO events, anomalous SST occurs off the coast of Ecuador, which then produces precipitation on the western Andean slope (Moy et al., 2002). This precipitation produced by the warm ENSO event creates debris-flow activity, increases stream discharge and sediment load in a stream entering Laguna Pallcacocha in the Southern Ecuadorean Andes, and deposits inorganic laminae. Moy et al. (2002) examined laminae and sedimentation rates in the sediment cores and determined the frequency of these climate-related events for 100-year non-overlapping windows (Fig. 6).

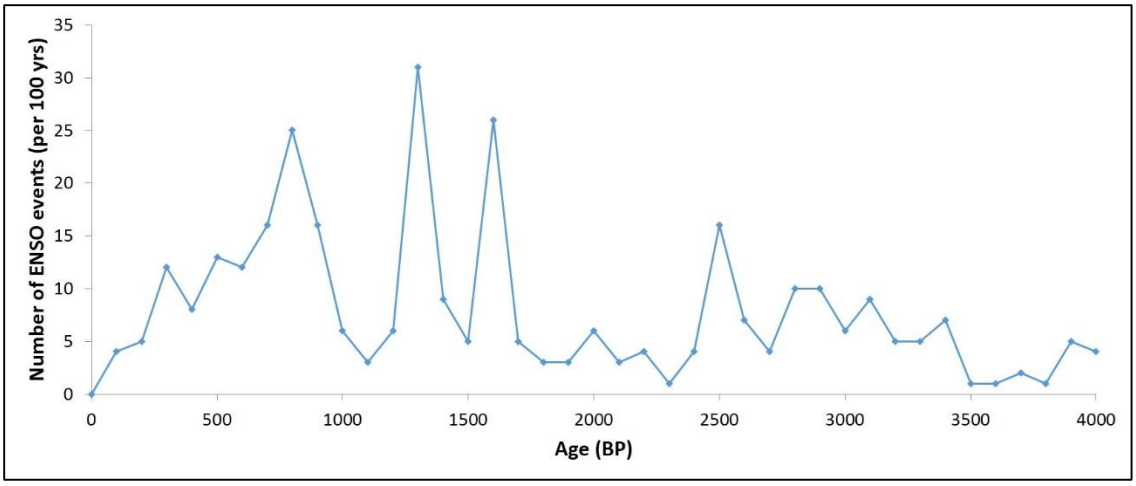

Fig 6. Number of warm El Niño/Southern Oscillation (ENSO) events in 100 year non-overlapping windows taken from the lake Laguna Pallcacocha (re-plotted form data of Moy et al., 2002). This lake is located at high altitude, east of the western Andean continental divide. It is a drainage basin covered in loose debris and debris-flow deposits (Moy et al., 2002). The frequency of ENSO events is used as a proxy for climate change. Times of warmer SST occur when the number of ENSO events is higher, which also brings more precipitation.

Using a constant carbon accumulation model, a time series for red color intensity in a sediment profile (Fig. 7) was created by Moy et al., (2002). The red color intensity shows different intensities and thicknesses of the dark organic-rich sediment and the light-colored mineral laminae from the sediment core. This climate proxy also illustrates the sedimentation rate at Laguna Pallcacocha. Although the number of ENSO events and color intensity values do not consistently track each other, they do show some correlations. For example, an increase in the number of ENSO events can correlate with an increase in red color intensity.

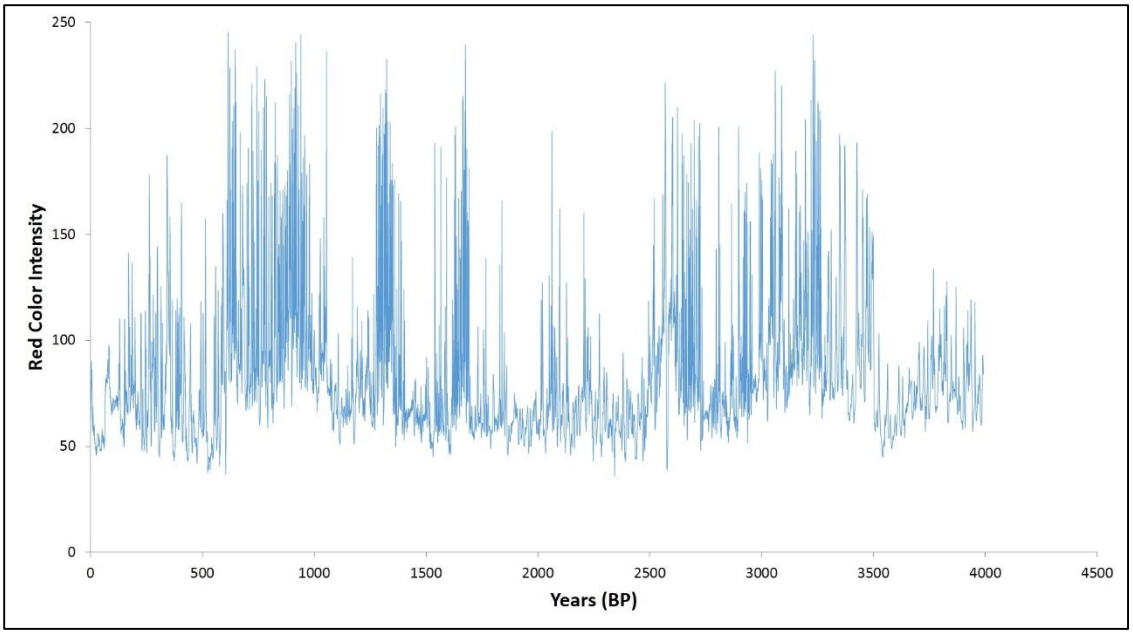

Fig. 7. Red color intensity time series quantifying the distribution and concentration of laminae in the Laguna Pallcacocha composite sedimentary record (re-plotted from data of Moy et al., 2002). Red color in the sediment profile is used as a climate proxy. The fluctuations of red color intensity were taken to indicate fluctuations in climate, and specifically the occurrence of El Niño/Southern Oscillation ENSO events.

A climate proxy study by Wallace and Anderson (2010) produced a proxy history of past intense hurricane impact for South Padre Island region in the northwestern Gulf of Mexico. The study examined cores collected from Laguna Madre, Texas, with results dating from approximately 5300 to 900 years BP. Grain size analyses were performed every 1 cm downcore for some segments of the cores and every 5 cm for other segments. Grain-size anomalies were taken to represent storm sediment deposits. The reported results from several cores were: approximately 6 major hurricane events between 4235-1582 years BP recorded in one core, 10 major hurricane events between 2382-1433 years BP recorded in a second core, 6 major hurricane events from 3558-940 years BP recorded in a third core, and 11 major hurricane events from 5377-2072 years BP recorded in a fourth core. Given that the sampling interval in the various cores represented anywhere from 12 to 135 years, it should be noted that the reported events may

actually have represented stormy periods rather than individual storms (Wallace and Anderson, 2010).

An additional northern Gulf of Mexico climate proxy was developed by Lane et al. (2011). The study compiled a 4500-year record of hurricane-induced storm surges from sediment cores collected from a coastal sinkhole lake near Apalachee Bay, Florida. Paleostorms were identified using sediment data and radiocarbon-based age models. Lane et al. (2011) reported that an average of approximately 3.9 intense storms per century had occurred. The greatest frequency of intense storm events occurred between 2800 and 2300 years ago, while fewer than 3 intense storms per century were reported to have occured between 1900 and 1600 years ago and between 400 and 150 years ago.

Two paleostorm proxy studies analyzing sediment cores from Lake Shelby along the Alabama coast, and Western Lake along the northwest Florida coast were reported by Liu and Fearn (1993; 2000). The sediment analysis from Lake Shelby suggested that a higher frequency of major hurricanes (Category 4 or 5) struck the Alabama coast around 3200-3000 years ago, 2600 years ago, 2200 years ago, 1400 years ago, and 800 years ago (Liu and Fearn 1993). The sediment core analysis from Western Lake suggested that from 3400 years BP to 5000 years BP and from 0 years BP to 1000 years BP, the area experienced periods of few major hurricanes. However, from 1000 years BP to 3400 years BP, the area was said to have experienced a "hyperactive" period of major storms (Liu and Fearn, 2000).

Another climate proxy record was developed by Marcott et al. (2013), employing 73 globally distributed records, including approximately 80% marine archives. These marine archives were produced by measuring Mg/Ca ratios in marine sediment cores taken from various locations in the global ocean. Using globally stacked temperature anomalies (referred to as the Standard5x5 reconstruction) (Fig. 8), cooling can be observed from mid- to late Holocene. The

result is said to be associated with temperature change in the North Atlantic (Marcott et al., 2013). The trends observed show correspondence between warmer conditions and wetter conditions. Although this study is not strictly specific to the Gulf of Mexico Region, it illustrates how temperature anomalies can affect climate. Of the 73 globally distributed temperature records used by Marcott et al. (2013), extratropical northern hemisphere mid-to-high latitude temperature record sets were part of the data set, and it was found that the North Atlantic section contributes most of the variance to the global signal. These extratropical northern hemisphere temperatures were even found to correlate with Asian monsoon intensity and the position of the Atlantic intertropical convergence zone (Marcott et al., 2013).

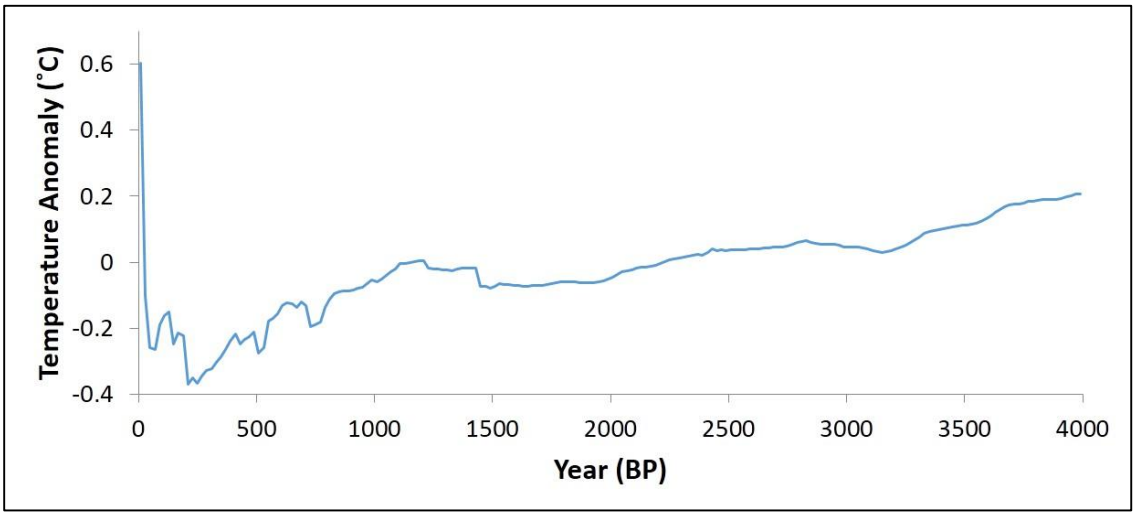

Fig. 8. Globally stacked temperature anomalies from a 5° × 5° area –weighted mean of 73 globally distributed temperature records based on a variety of paleotemperature proxies (re-plotted from data of Marcott et al., 2013). The global temperature anomaly curve illustrates the relation of modern temperatures to temperatures over the past 4,000 years. Zero represents the 1961-1990 AD instrumental mean.

A 2000-year upper ocean salinity proxy was constructed for the northeastern Caribbean by Nyberg et al. (Fig. 9), using δ18O analyses of planktonic foraminifera and an artificial neural network (ANN). The ANN was trained on a modern data base of planktonic foraminifer census data, and oxygen isotope ratios of Globigerinoides ruber to reconstruct the SST and sea-surface salinity (SSS) fluctuations (Nyberg et al., 2002). In the Sargasso Sea, G. ruber has been shown to

record annual mean SST and SSS (Nyberg et al., 2002). In this study, lower sea surface salinity values were found to correspond with drier periods in Mexico, while higher salinities correspond with wetter climate (Nyberg et al., 2002). This proxy provides additional evidence regarding regional climate history.

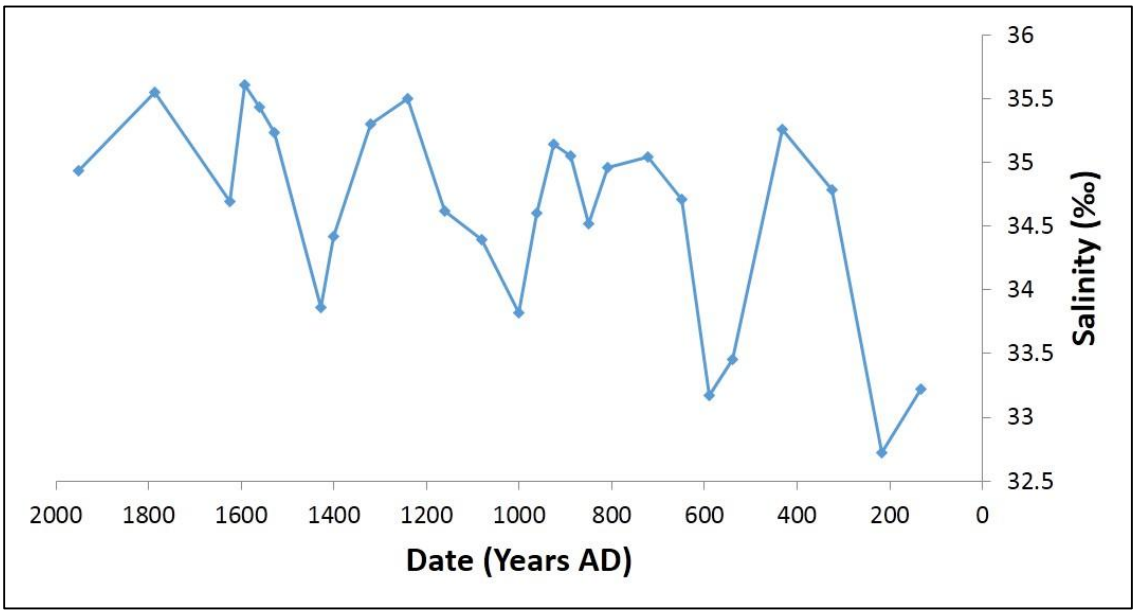

Fig. 9. Paleo-salinity proxy record for the Caribbean, based on oxygen isotope values of *Globigerinoides ruber* from a core retrieved from the northeastern Caribbean (re-plotted from data of Nyberg et al., 2002).

A study by Esper et al. (2002) examining long tree-ring records provides a climate proxy for the extratropical region of North America (Fig. 10). When investigating ring widths of trees growing in cooler climates, the width will usually reflect the influence of warm-season temperatures on growth, and also may reflect temperatures during the cool-season. Esper et al. (2002) used regional curve standardization chronology (RCS) to analyze the raw ring-width measurements. Although these data do not date as far back as other proxies, they nonetheless provide some insight to climate trend in the North America extratropical region. Evidence for above-average temperatures during the "Medieval Warm Period" (approximately 1050 to 750 years BP) can be inferred, as well as large-scale warming after the year 1850 (Esper et al., 2002).

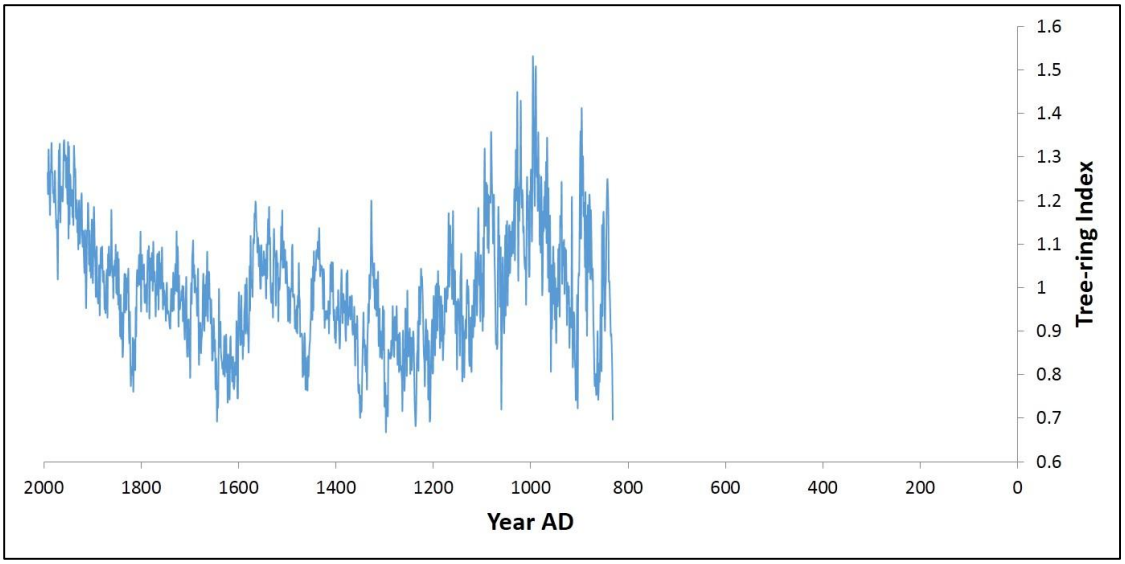

Fig. 10. Tree-ring index for the Northern Hemisphere extratropical region (re-plotted from data of Esper et al. 2002). The curve was generated by analyzing the individual raw ring-width measurements using Regional Curve Standardization (RCS). This climate proxy relates higher tree ring index values to warmer climate.

Two climate proxies constructed by Richey et al. (2007) dating back approximately 2,000 years were from a core taken in the Pigmy Basin in the northern Gulf of Mexico. The proxy (Fig. 11) was created from isotopic and elemental analysis of the foraminifera G. ruber white variety, and is similar to the salinity proxy of Nyberg et al. (2002). Richey et al. (2007) then converted the Mg/Ca to an SST estimate. Using a G. ruber – specific equation with a fixed exponential constant where:

$$[Mg/Ca = 0.499 \exp(0.09\ SST)]$$

Richey et al. (2007) was able to convert Mg/Ca to SST. A higher Mg/Ca ratio corresponds to a higher SST.

By analyzing Mg/Ca of G. ruber, sea surface temperatures in the Gulf of Mexico (Fig. 11) between 1000 and 1400 yr B.P. were found to be nearly as warm as modern conditions (Richey et al., 2007). Richey et al. (2007) found a correspondence between sea surface

temperatures in the Gulf of Mexico and changes in solar insolation. When compared to Esper et al. (2002) tree ring results, similarities can be found between the two studies such as comparing increasing trends in tree ring index with increasing trends in SST.

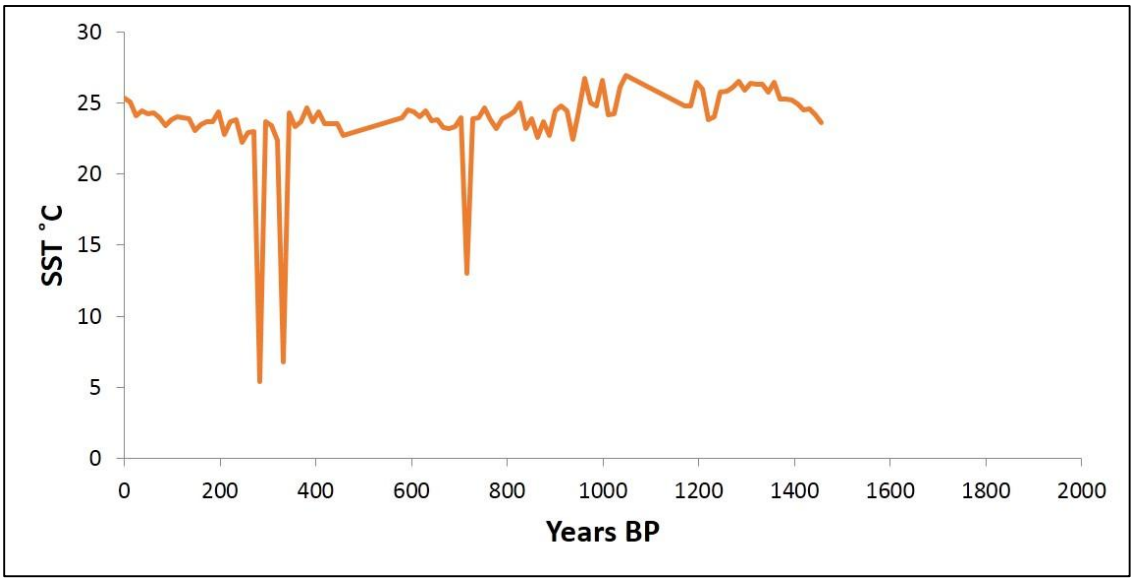

Fig. 11. Sea-surface temperature (SST) proxy data for northern Gulf of Mexico (re-plotted from data of Richey et al., 2007). The sea-surface temperatures were obtained by analyzing Mg/Ca of *Globigerinoides ruber*. Mg/Ca values are used as a climate proxy, with higher values correlating to warmer SST. The SST curve illustrates the changes in climate during the past 1,500 years. Warmer SSTs correlate to warmer air temperatures.

1.5 Hypotheses

Sea level in the Gulf of Mexico has fluctuated throughout the late Holocene. This has been made evident in previous proxy studies, which have reported high-stands during the late Holocene. Walker et al. (1995) and Stapor et al. (1991) found evidence for sea-level highstands in the northern Gulf of Mexico between 3,000 and 1,000 years ago, with rises of as much as 2 meters above present sea level. Balsillie and Donoghue (2004) also found several sea-level fluctuations of +/-1 meter over the past 6,000 years (Fig. 12). The principal hypothesis driving this investigation was that climate proxies for a coastal region of the northern Gulf of Mexico should reflect the regional, and perhaps global, climate fluctuations -- including sea-level change

-- during the late Holocene. An ancillary hypothesis was that ground-penetrating radar (GPR) data from an extensive beach-ridge plain can be employed as a proxy for sea-level change. In this study, GPR data from a survey transect on St. Vincent Island was used to establish a new sedimentologic proxy for sea-level change. The goal of this study was to develop this new paleo-sea level proxy, which was compared with previous sea-level proxies of the northeastern Gulf of Mexico and surrounding areas. In addition to creating a paleo-sea-level proxy, a second climate proxy was established. A paleo-storm proxy was developed using sediment analysis, obtained by a laser particle analyzer, of a sediment core taken from Oyster Pond on St. Vincent Island. This paleo-storm proxy was compared with previous paleo-storm records from the region. Both the grain size data and GPR data should be correlated as climate proxies. Additionally, these data were correlated with other regional proxy climate data. Using this new sea level and paleo-storm proxy data, the relationship of past and future climate and sea level can be better understood.

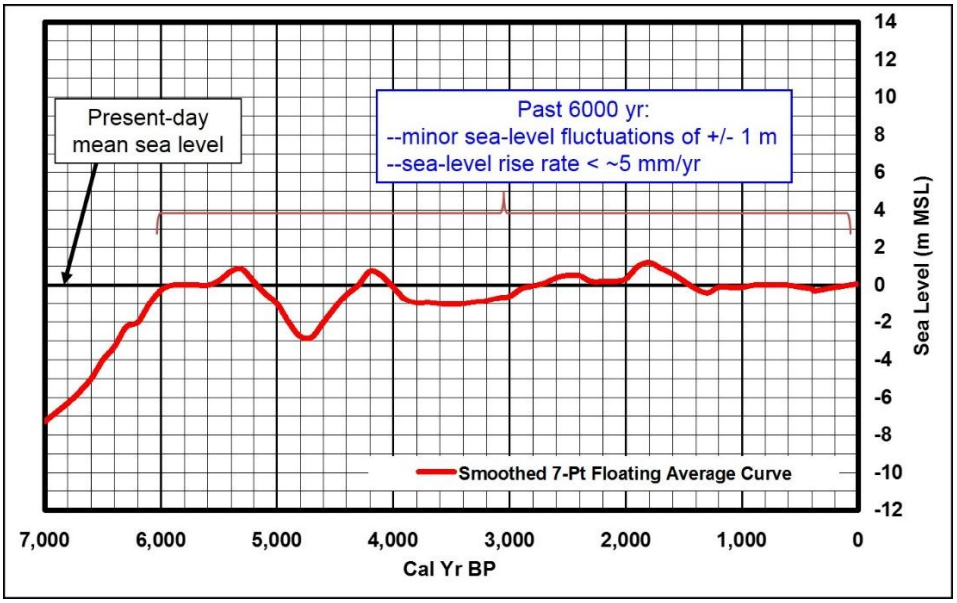

Fig. 12. Sea-level history for the Gulf of Mexico over the last 7,000 years. Figure from Balsillie and Donoghue (2004).

CHAPTER II

METHODS

This section explains the methods used to collect and analyze the GPR data and sediment texture data. Also, the process by which the chronology of Oyster Pond core 092710-01 was determined is explained**.**

2.1 GPR Transects and Analysis Methods

Ground penetrating radar (GPR) is a noninvasive remote sensing technique that detects discontinuities in the shallow subsurface. Two antennas are placed on the ground, a transmitting antenna and a receiving antenna. The transmitting antenna sends pulses of electromagnetic energy into the subsurface (Neal, 2004). When these pulses reach a given geologic feature in the subsurface, the pulses reflect back to the surface, and the data are collected by the receiving antenna (Fig. 13). The measurement that is being collected by the receiving antenna is the time it takes for the electromagnetic waves to be transmitted, reflected, and received. Low frequency antennas (in this study, 50 MHz) collect data reaching deeper depths, but have lower resolution. High frequency antennas (250 MHz) collect data for shallower depths, but at higher resolution. GPR has commonly been used in sedimentology to determine past sedimentary processes and also to reconstruct depositional history (Neal 2004).

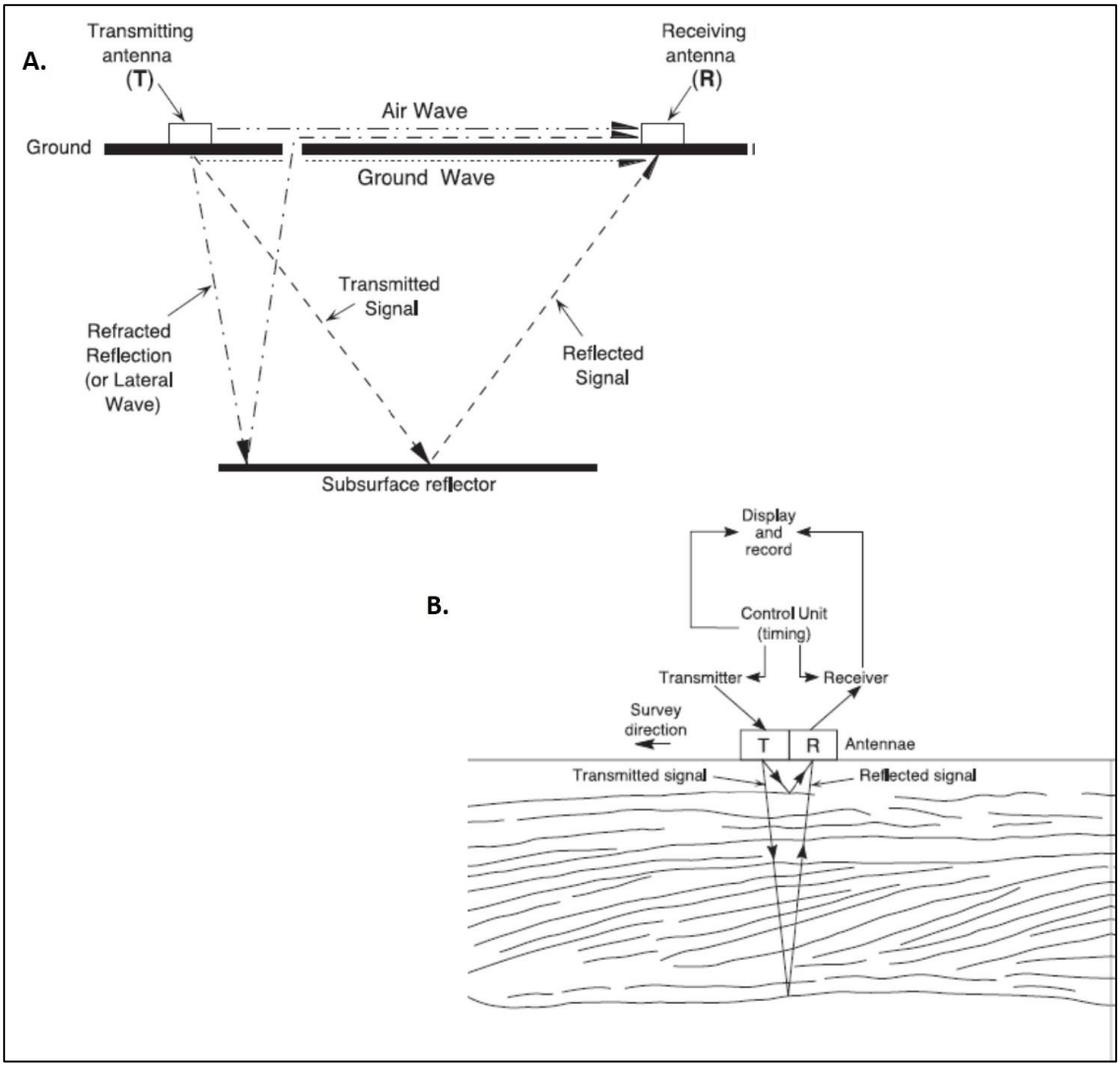

Fig. 13. Illustrations of GPR data acquisition. A.) Ray paths for the airwave, ground wave, lateral wave, and reflected wave. B.) Data acquisition at an individual survey point (adapted from Neal, 2004).

The equipment used to collect the GPR data for this study was a Mala GPR model CU-II system, using both the 50 MHz and 250 MHz antennas. Data collection consisted of both north to south transects, and south to north transects along Road 4 on St. Vincent Island (Fig. 2). The GPR's GPS unit was not recording during the time of the survey, and so a hand-held GPS was used to record the position at various locations and a wheel to record the distance, primarily where the island roads crossed.

In order to process and analyze the data, the MAT-GPR program was used, along with RADAN GPR (v. 6.6) processing software. Prior to processing the data in MAT-GPR, equally spaced traces were needed to apply frequency wavenumber (F-K) migration and filters. This was accomplished by applying a migration in the RADAN software. After the migration in the RADAN software was completed, using the MAT-GPR program, several steps were taken to obtain the final processed data. For the 50-Mhz transects, the first step was to apply a low-pass F-filter passing at 0.76 GHz. This cuts off any extra frequencies (extraneous high frequency data) that may be present. Next, the time window was trimmed. This needed to be done after frequency filtering because noise tends to stay at the bottom of the time window. The noise at the bottom of the window is not true data, and is the time data due to interference of the signal. After trimming the time window, an AGC gain of 50 was applied, followed by an F-K migration. The final step was to apply a down-dip F-K filter. The F-K filtering removes any features dipping opposite to the desired results (Neal, 2004). This study is only interested in the reflectors dipping toward the Gulf of Mexico shoreline. For the 250-Mhz transects, there were two steps that varied from the 50-Mhz transects. Instead of applying a low-pass frequency filter, a band pass frequency filter was applied. The band pass was chosen from the middle of the window, with a band range of 0.72- 0.32 GHz. The second difference involved the AGC gain. Instead of using a gain of 50, an AGC gain of 5 was used. This was used because of the use of a different sampling interval in the 250-Mhz antenna compared to the 50-Mhz antenna. The order in which the steps were performed remained the same with the 250-mhz data as they were with the 50-Mhz data.

After the GPR data were processed, paleo-sea level was interpreted based on the GPR signature. Beach ridges in the subsurface can be seen as seaward dipping bounding surfaces, with the dip of the reflectors decreasing in a seaward direction. The basis for using beach-ridge GPR data as a sea-level proxy is the assumption that the toe of the paleo-beach ridge represents a paleo-sea level position, specifically the low-tide sea level. All of the reflectors indicating the

paleo-beach ridges dip seaward. The interpretation of paleo-sea level, evidenced by the location of the beach-ridge toe in the subsurface, is shown in Fig. 14.

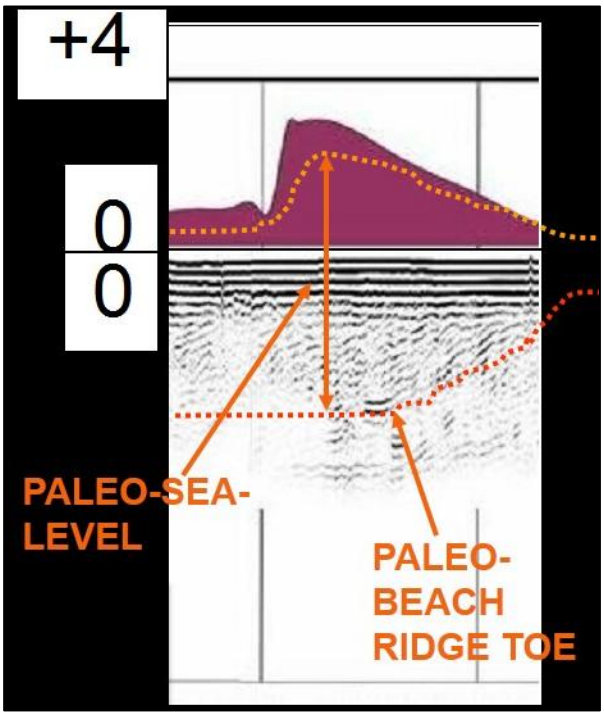

Fig. 14. Interpretation of paleo-sea level from GPR data, showing the location of the plaeo-beach ridge toe, and how it compares to the present-day beach ridge. Seaward direction (south) is to the left (modified from S. Kish unpublished data).

2.2 Sediment Texture Analysis

For sediment textural analysis, a Cilas 1180 laser particle analyzer was used to determine grain size in phi (Ø) units, percent sand, percent silt, percent clay, moment skewness, moment standard deviation, along with the grain diameters (in micrometers) at 5%, 7%, 10%, 16%, 50%, 84%, 90%, 95%, and 98%. A sediment core, 80.5 cm in length, taken from Oyster Pond (core 092710-01) was sampled at 0.5 cm intervals. The sampling location is shown in Fig. 4. Approximately 0.5 grams of each sample was mixed with 50 mL of a dispersant (de-ionized water and 0.5% sodium metaphosphate) using a magnetic stirrer in a 200 mL beaker. As the sample was being actively stirred and the particles were in suspension, approximately 5 mL of the

sample was extracted from the beaker, and then injected into the laser particle analyzer. The grain size statistics were then determined using the Folk and Ward (Folk, 1974) statistical methods.

Each 0.5 cm interval sample was injected into the Cilas instrument and analyzed a minimum of two separate times. This procedure was executed in order to obtain repeatability within the sample. In some cases, the same sample had to be processed in the Cilas laser particle analyzer a third time, due to anomalous values or processing errors. After collecting the multiple sets of data for each sample interval, the values were averaged, resulting in 161 sample average values. All individual data parameters were averaged and viewed in profile plots using Microsoft Excel. These averages were obtained from the individual repeatable pairs.

X-radiography was carried out on the entire 80.5 cm of the core and shows a few of the more obvious sand layers within the generally mud-rich core. The sand laminae are taken to represent storm events or periods of greater-than-average storminess. The higher resolution and sensitivity of the laser particle analysis enables more sandy laminae to be distinguished than are visible by eye or x-radiograph.

2.3 Sediment Core Chronology

Seventeen samples were collected from Oyster Pond core 092710-01 to establish core chronology using the lead-210 method. In the upper 25 centimeters, the sampling interval was every two centimeters. From 25 centimeters to 45 centimeters downcore, the sampling interval was every 5 centimeters. The samples were obtained by wet-sieving to collect the fine samples, dried, and ground into a powder. After the parent isotopes (Pb-210) and daughter isotopes (Po-210) were sealed in a container and allowed to equilibrate for one month, the samples were then placed in a gamma counter for 3 to 10 days. Similar to the method of Kim and Burnett (1983),

the samples underwent gamma spectrometry at the Environmental Radioactivity Measurement Facility at Florida State University.

Two C-14 ages were obtained from the Oyster Pond core 092710-01. These ages from organic sediment were collected at 52.5 centimeters and 75 centimeters downcore. The two ages were then calibrated using the CALIB 7.0 carbon 14 dating program (CALIB, 2013). The program provided calibrated ages plus one sigma and two sigma limits on the age of the samples.

CHAPTER III

RESULTS

In this section, the results of the GPR data will be examined. The sediment texture data will also be described, along with the core chronology of Oyster Pond core 092710-01.

3.1 GPR Data

The GPR transect was conducted so that it would cross the majority of the beach ridge sets near the center of the island, in a north-south direction, as shown in Fig. 2. The beach ridge GPR data were used to determine the subsurface depth to the toe of the ridge, at the point where the ridge profile changes inflection and shallows out. Figure 15 illustrates the raw GPR data and processed GPR data. The interpretation of the beach-ridge toes can be seen in Figure 16. An example of the St. Vincent Island GPR data is shown in Fig. 17. The data are taken from the transect segment running from north to south using a 50 MHz antenna. The transect location is also shown in Fig. 2. Figure 18 is from a transect segment taken from north to south using a 50 MHz antenna. The beach ridge shown in the figure is located at approximately 25 meters along the transect. Figure 19 overlays a topographic profile of Road 4 above a GPR transect of Road 4. The topographic beach ridges can be seen to correlate with the subsurface expression of the beach ridges (Fig. 14). A 50 MHz antenna was also used in Fig. 19.

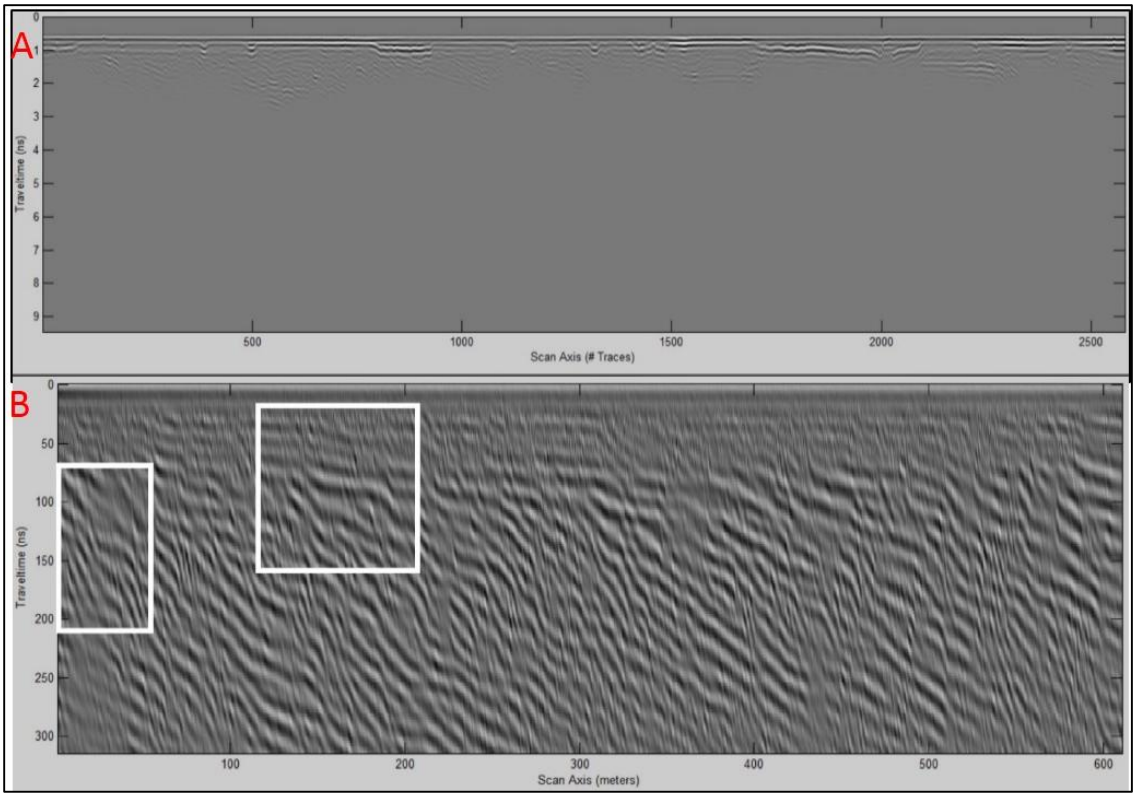

Fig. 15. A) Unprocessed ground-penetrating radar (GPR) transect along Road 4; B) Processed GPR transect of (A) indicating examples of beach-ridge toes outlined by the white boxes (note vertical scale change). Interpretation of beach-ridge toes in highlighted rectangles can be seen in Fig. 16.

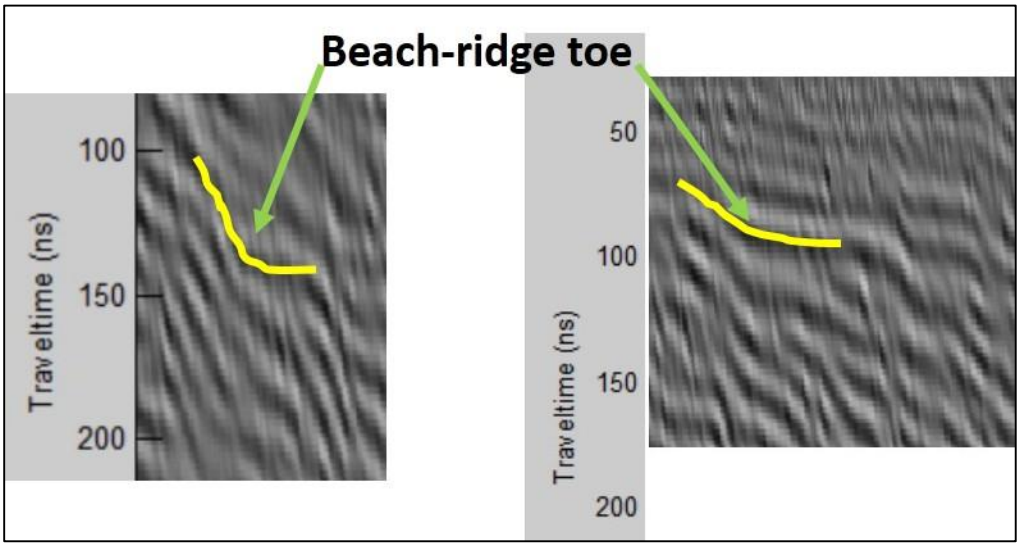

Fig. 16. Examples of ground-penetrating radar (GPR) data showing the interpretation used to identify beach-ridge toes from highlighted locations in Fig. 15.

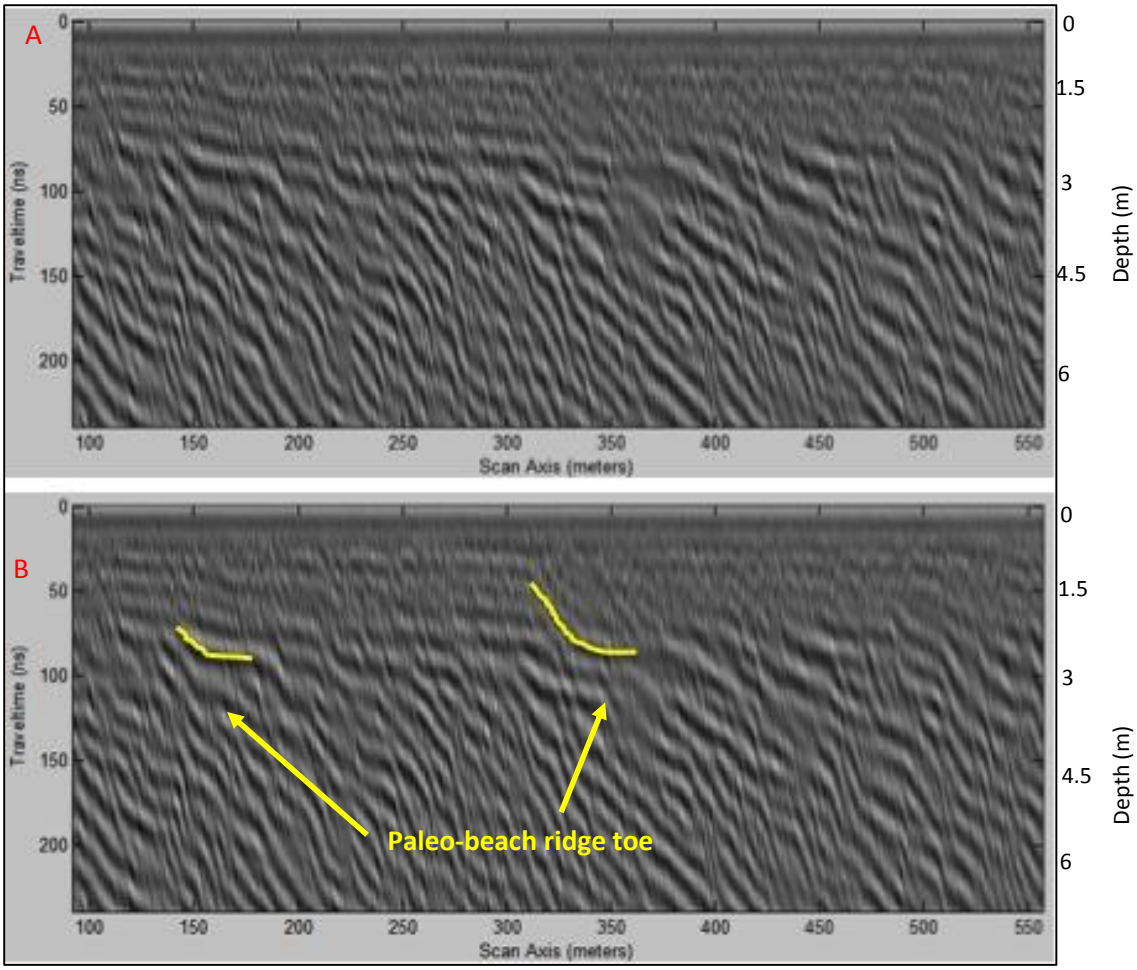

Fig. 17. Example of ground-penetrating radar (GPR) data. A.) Processed GPR data; B.) Interpretation of subsurface expression of paleo-beach ridges, represented by the yellow lines. Approximate location of the transect is represented by the orange X shown in Fig. 2. South (seaward) is to the right.

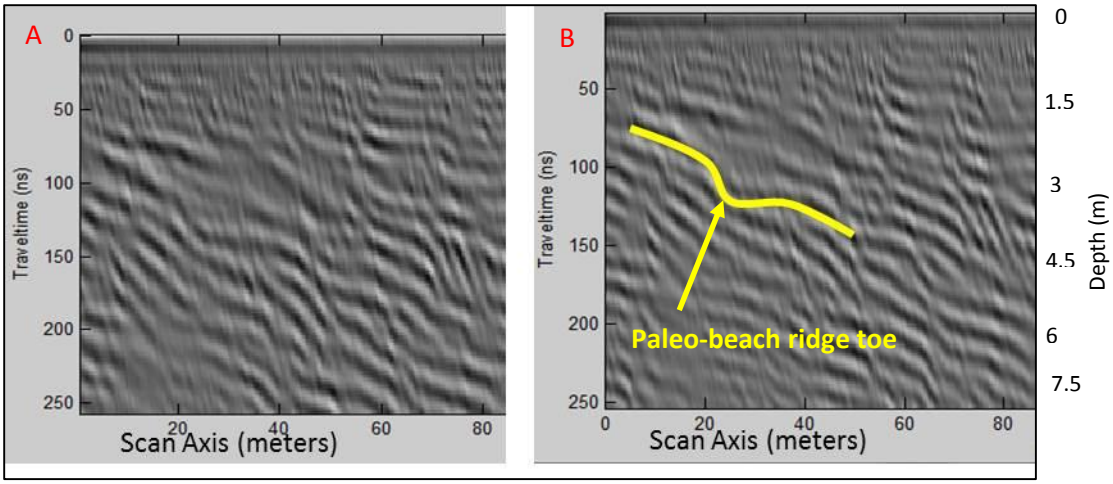

Fig. 18. Example of ground-penetrating radar (GPR) data. A.) Processed GPR data; B.) Interpretation of a paleo-beach ridge, represented by the yellow line. Approximate location of the transect is represented by the green X shown in Fig. 2. South (seaward) is to the right.

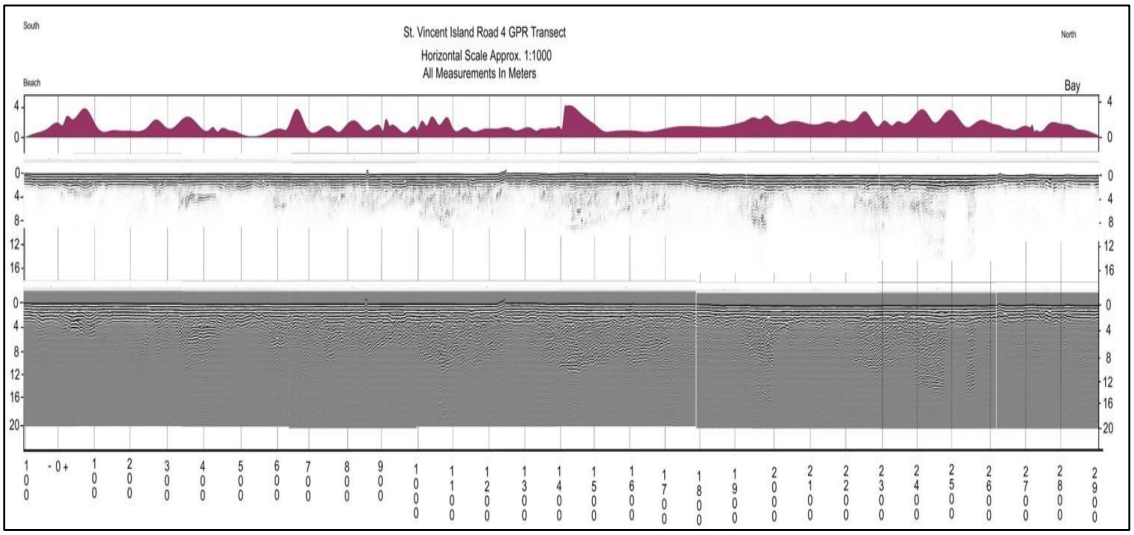

Fig. 19. Full length topographic and ground-penetrating radar (GPR) profile of Road 4 on St. Vincent Island. The top section illustrates the beach ridge topographic survey, with elevations shown in meters above sea level. The middle (filtered) and lower (unfiltered) sections illustrate the GPR transect profile. The y-axis in the lower two sections represents subsurface depth in meters, and the y-axis in the top section represents the height above current sea level of the beach ridges. The x-axis represents the south-to-north length of the transect in meters. The seaward direction (south) is to the left (from S. Kish, unpublished data).

In order to determine the ages of the ridges, a previously-obtained set of optically stimulated luminescence (OSL) dates on selected beach ridges was employed (Forrest, 2007).

Table 1 displays the data set. There were six OSL dates used in determining the ages of the paleo-beach ridges.

After converting GPS coordinates to Universal Transverse Mercator (UTM) coordinates and combining 50-Mhz and 250-Mhz GPR data, a curve was created, showing the GPR depth (in two-way-travel time) of the basal beach ridge deposits in relation to distance along the transect on St. Vincent Island (Fig. 20). This represents a profile of the GPR data for the period when the individual beach ridges were the actively prograding front of the barrier island. The total length of the GPR data set was approximately 3000 meters from north to south on Road 4, with the first paleo-sea level data point recorded between Road G and Road F and the last paleo-sea level data point near the Road A intersection (Fig. 21). The OSL ages from Table 1 were transposed to the appropriate location along the GPR transect where the dated beach ridges intersect the transect. Ages were determined for each of the paleo-sea-level proxy locations by interpolating between ridges with known OSL ages.

Table 1. St. Vincent Island beach-ridge ages.

UTM Coordinates		Sample	---------- Distance ----------			OSL Age
Easting	Northing	Site No.	From	To	(m)	(ka)
686090	3284110	SVI-015	-	-	0	4.1+/-0.3
681337	3283301	SVI-002	SVI-015	SVI-002	2555	3.5+/-0.3
681246	3282625	SVI-003	SVI-002	SVI-003	682	2.5+/-0.2
680714	3282056	SVI-004	SVI-003	SVI-004	779	2.5+/-0.3
678618	3281906	SVI-023	SVI-004	SVI-023	1350	1.2+/-0.1
679150	3280692	SVI-025	SVI-023	SVI-025	852	0.8+/-0.1

NOTE: Figure 2 shows the approximate locations of the beach ridge sampling site numbers.

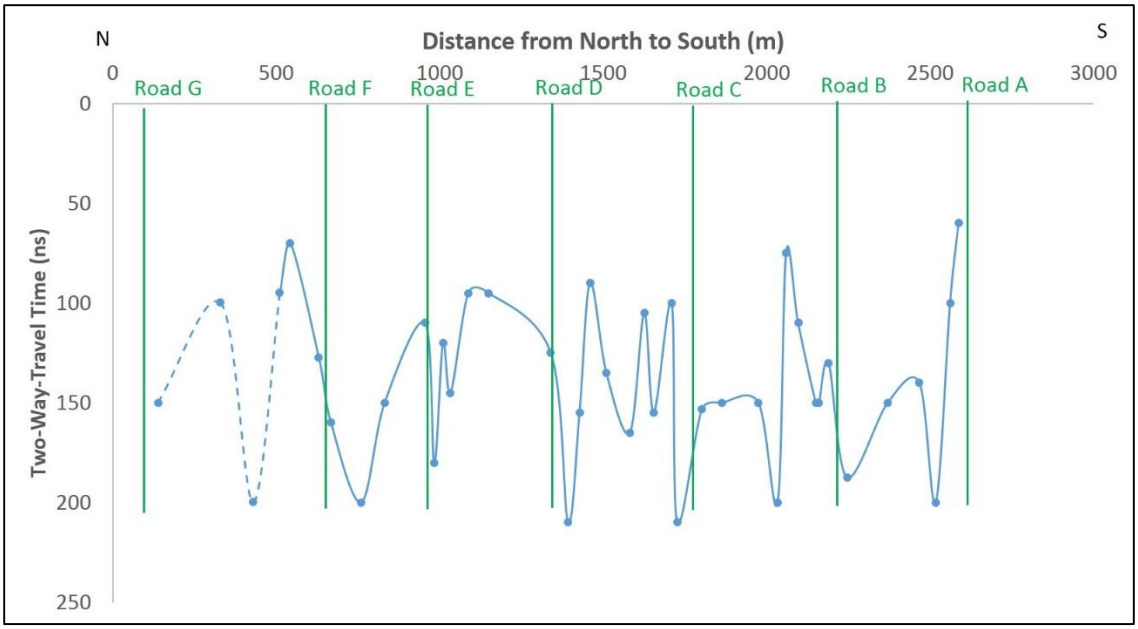

Fig. 20. Ground-penetrating radar (GPR) proxy data profile from north to south through St. Vincent Island beach ridge plain. Data represent the depth of the toe of the paleo-beach-ridge imaged in the subsurface by GPR. South (seaward direction) is toward right. Location of transect is shown in Fig. 2. Dashed lines represent poor data quality. Locations of Roads A through G are indicated by the green lines and can be seen in Fig. 21.

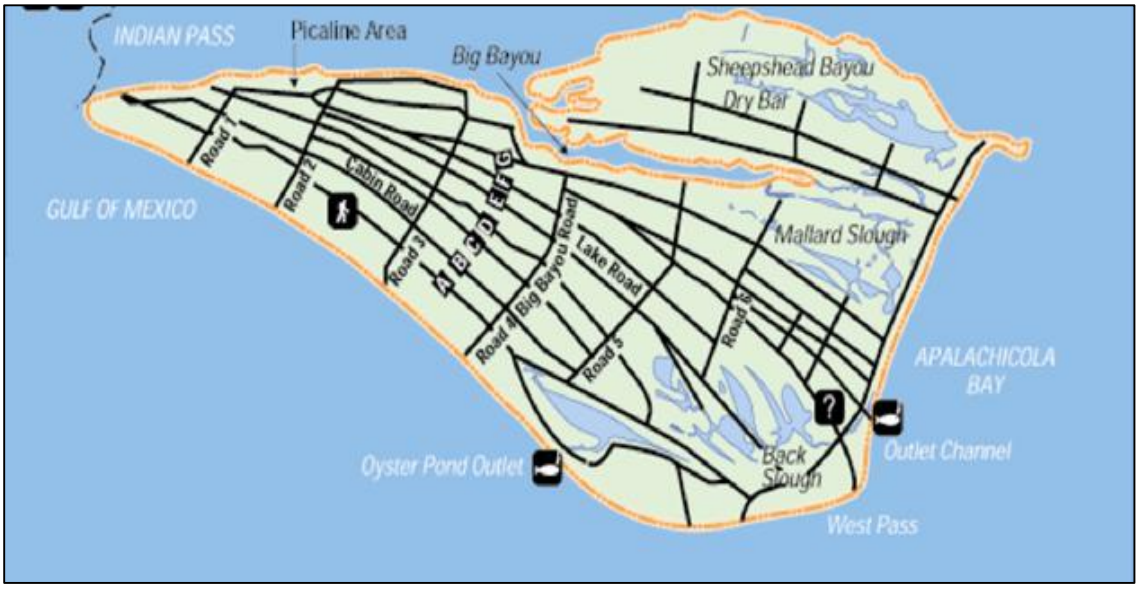

Fig. 21. St. Vincent Island study area, showing location of Road 4 (Big Bayou Road) intersecting with Roads A-G. Location of intersections along GPR transect can be seen in Fig. 20. Figure from St. Vincent Island National Wildlife Refuge.

In order to convert the two-way-travel-time in nanoseconds to meters, the radar response velocity for the surface material needed to be known. The surface material in this case varies between dry sand and saturated sand. Radar velocity in dry sand is 0.15 m/ns, while that of saturated sand is 0.06 m/ns, and that of seawater is 0.01 m/ns (Fisher et al., 1992). For the current investigation, a value of 0.03 m/ns was used, approximately midway between that of saturated sand and seawater, on the assumption that much of the subsurface of the island is saturated with brackish water. Using a constant radar velocity to calculate the time-to-depth conversion was also previously reported in a study on a barrier island in the northwest Gulf of Mexico (Garrison et al., 2010). The GPR survey was found to penetrate approximately 8 meters depth below the surface. The GPR signal, on average, began to disappear at approximately 5 meters depth below the island surface. After converting two-way-time in nanoseconds to depth in meters, the subsurface values were then corrected for the actual height above sea level at each point. To do this, data from a topographic survey along Road 4 were used. The values for elevation above sea level for the locations on the topographic transect were then subtracted from GPR depth values. The end result was a proxy sea-level curve based on the distance along the transect and the depth of the basal portion of beach ridges in the subsurface (Fig. 19). The depth of the paleo-beach ridges in the GPR profile range from approximately 1 meter to almost 5 meters below the ground surface. The depths were then corrected for ground surface elevation to determine the elevation of the paleo beach-ridge plain relative to present-day sea level (Fig. 22). This depth below present sea level is represented by the y-axis in Figure 22.

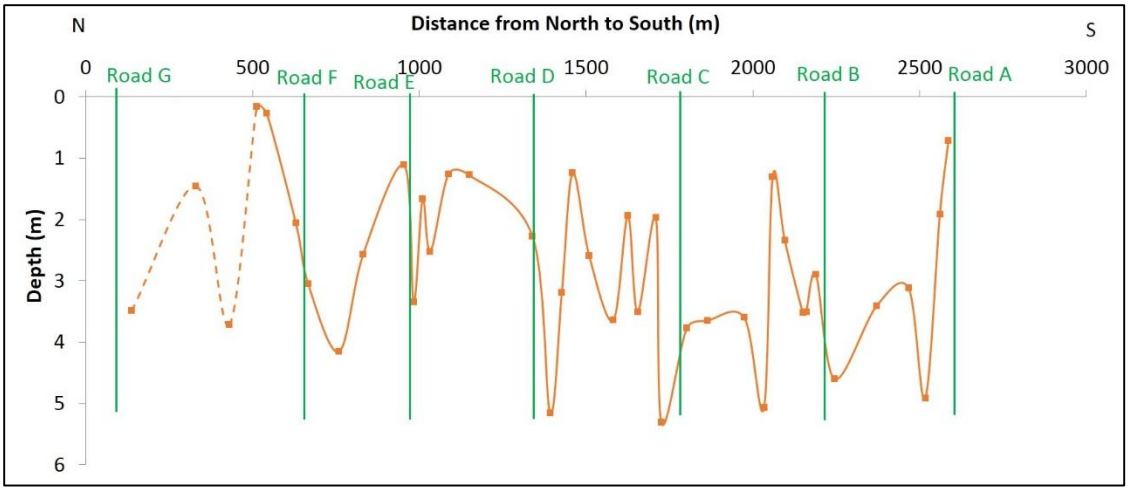

Fig. 22. Translation of ground-penetrating radar profile from Fig. 20 into elevation relative to present-day sea level, after correction for ground surface elevation. Two-way-travel time has been converted to meters below present sea level. Data represent the depth below sea level of the toe of each paleo-beach ridge. South (seaward direction) is toward right. Location of transect is shown in Fig. 2. Dashed lines represent poor data quality. Locations of intersections of Roads A through G are indicated by the green lines and can be seen in Fig. 21.

3.2 Sediment Texture Data

Data obtained from the laser particle size analysis are shown in Figure 23. Particle sizes are reported in phi units, where:

$$Ø = -log2d$$

and d is the grain diameter in millimeters. Thus, a smaller phi size indicates a larger mean grain diameter. The data show that mean grain size increases as percent sand increases. Anomalies within the sediment texture data indicate possible periods with greater or lesser frequency of intense storms.

In addition to mean grain size and percent sand, the average diameter in µm at 5%, 10%, and 98% were analyzed, as well as the average moment skewness. These data sets are tabulated in Appendix A. Similar to the anomalies in percent sand and mean grain size, anomalies in the graphs of the average diameter in µm at 5%, 10%, and 98%, as well as the average moment

skewness were evaluated to determine if they also might serve as indicators of periods of greater or lesser frequency of intense storms. Upon reviewing and studying all of the different parameters, percent sand and mean grain size were determined to be the best textural parameters to focus on.

The textural parameters used to develop the storm model are shown in Figure 23. The percent sand values range from 0% sand to 96% sand, with a mean of 34%. The mean grain size values range from 2.5 Ø to 6.6 Ø, with a mean of 4.9 Ø. The anomalies seen in the percent sand and mean grain size profiles correlate with many of the more obvious sand layers seen in the x-radiograph.

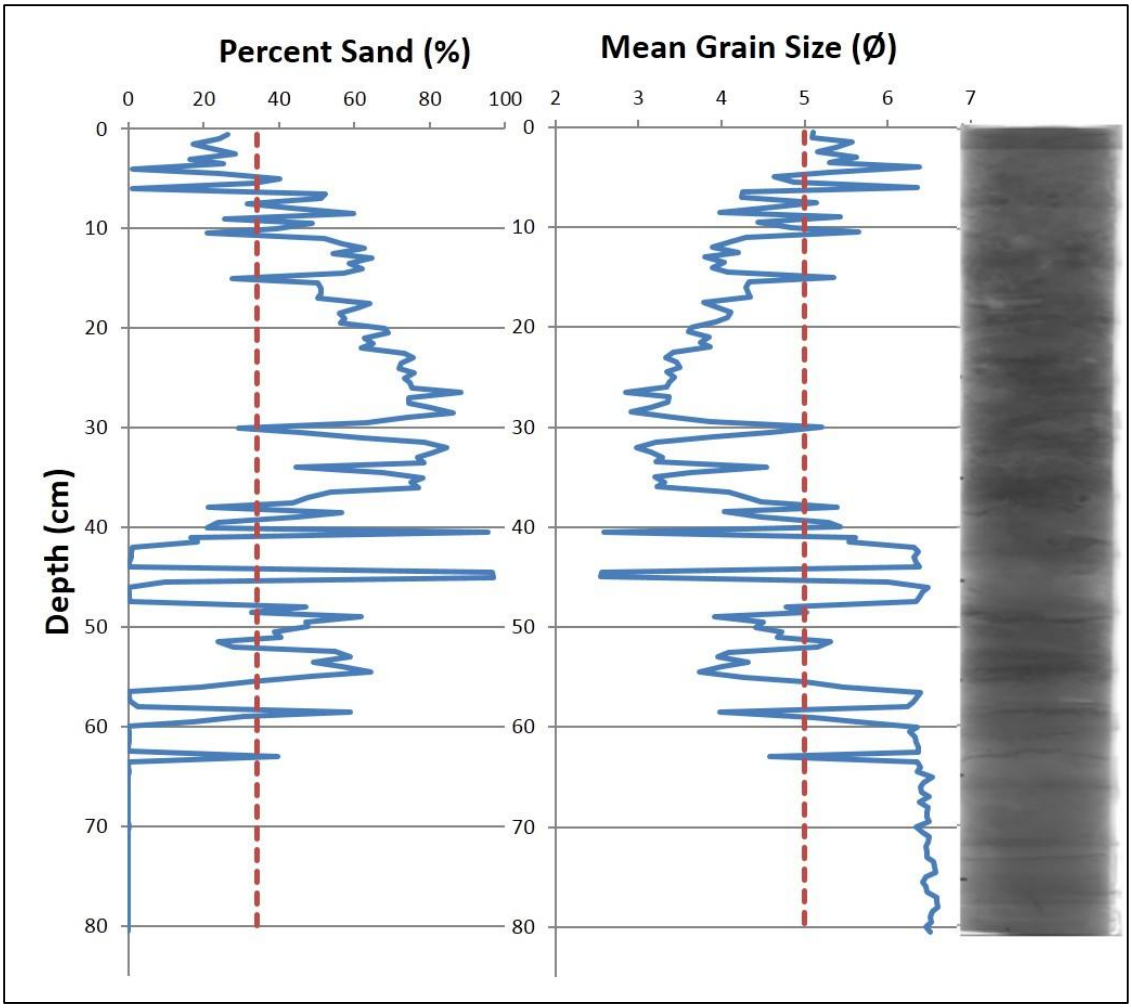

Fig. 23. (Left) Results of sediment analysis for Oyster Pond core 092710-01. Average percent sand and average mean grain size are represented by the dashed red lines. X-radiograph for core 092710-01 is shown at right. Core length is 80.5 cm.

3.3 Sediment Core Chronologic Data

To determine the age and sedimentation rate of the core, Pb-210 dates were obtained for the upper 41.5 cm of the core. The Pb-210 activity data were analyzed using the constant rate of supply (CRS) model, resulting in the age-depth profile shown in Figure 24. The CRS model assumes that Pb-210 input is constant each year, but the annual amount of new sediment can vary (Appleby and Oldfield, 1978; Coor, 2012). The Pb-210 date showed a decrease in sedimentation rate progressing from the top of the core to 41.5 cm. From 0.5 cm to 32.5 cm, each centimeter

represented an average of 1 to 2 years. From 32.5 cm to 41.5 cm, the sedimentation rate decreases, and each centimeter represented increasingly longer span of years, with an average of approximately 10 years per centimeter. The lower end of the Pb-210 chronology represents about 1854 AD, at 41.5 cm.

Below 41.5 cm, two radiocarbon dates were determined. At 52.5 centimeters a calibrated age of 1886 +/-19 cal BP years and at 75 centimeters an age of 1610 +/-18 cal BP years were obtained on organic mud. The inverted ages could be due to material, such as roots, pulled into the bottom of the core during retrieval. Therefore, only the C-14 age at 52.5 centimeters was used to establish core chronology below 45 centimeters. A constant sedimentation rate, representing approximately 162 years per centimeter was used for the remainder of the sediment core below 41.5 cm (Fig 25).

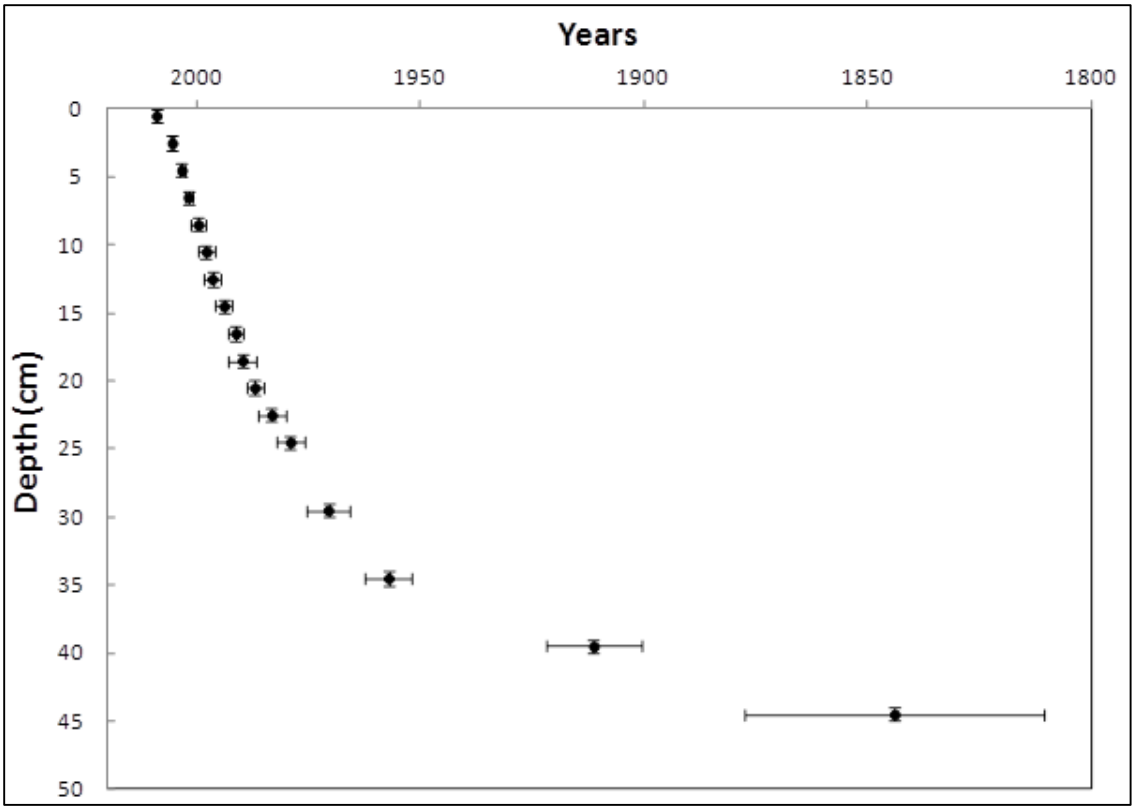

Fig. 24. Age-depth profile from the constant rate of supply (CRS) model of the Pb-210 data. Vertical bars represent the interval samples, and horizontal bars represent the age uncertainty (from Coor 2012).

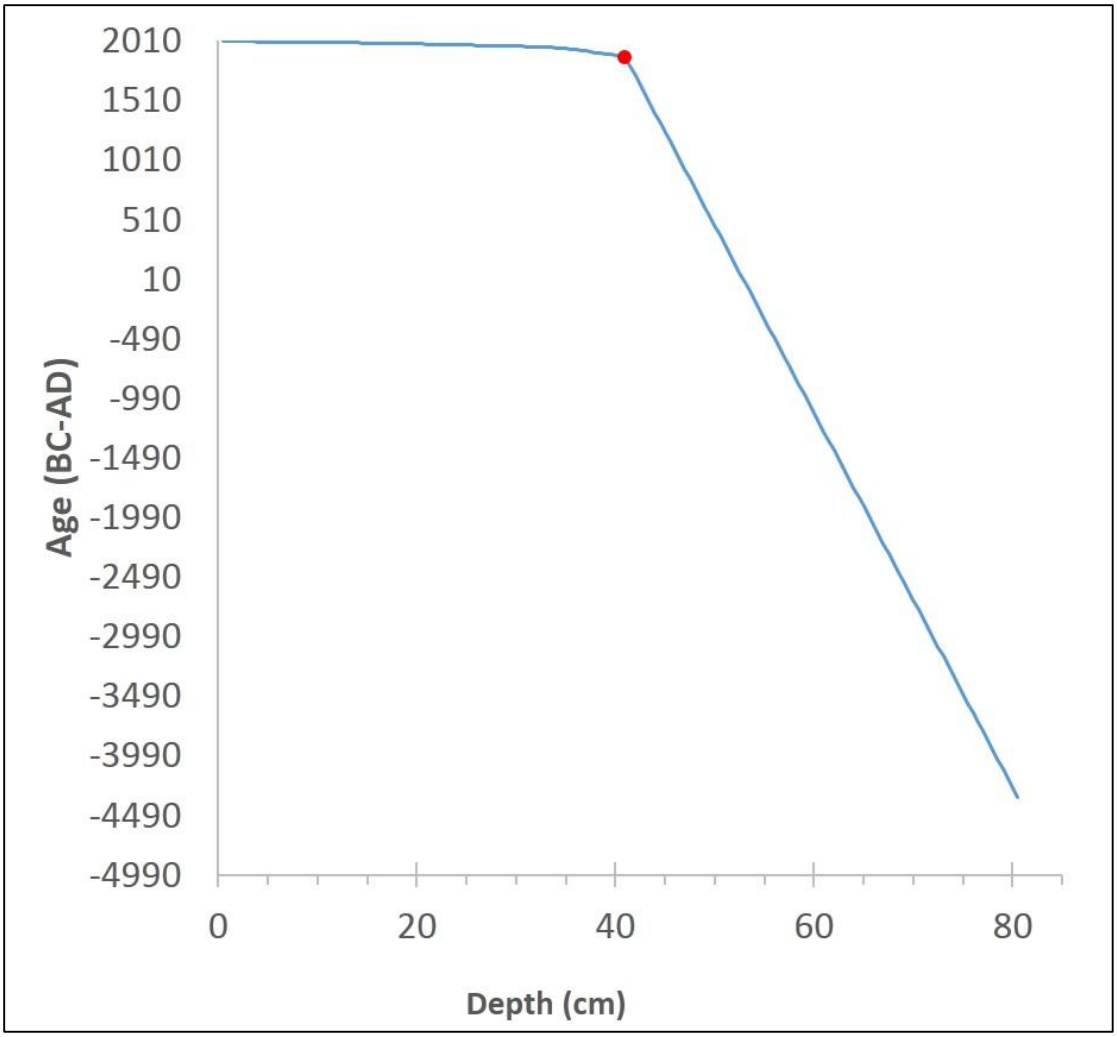

Fig. 25. Age-depth profile combining the Pb-210 dates with the C-14 date used. The C-14 date is indicated by the red dot. The ages to the right of the C-14 date were determined

CHAPTER IV

DISCUSSION

This section describes the meaning of the GPR and sediment texture data results. A paleo-sea level curve for the northeastern Gulf of Mexico created from the GPR data will be developed and examined. Additionally, a storm model will be employed to create a paleo-storm proxy for the northeastern Gulf of Mexico. The paleo-sea level curve and paleo-storm proxy created in this study will then be compared to additional proxies form the region.

4.1 Interpretation of GPR data

When examining GPR data of beach ridges, the beach ridges in the subsurface can be identified as seaward-dipping bounding surfaces, with the seaward-dipping reflectors decreasing in dip in a seaward direction (Neal et al., 2002; Forrest, 2007). Once paleo-sea levels were identified throughout the St. Vincent Island GPR data, the elevation of paleo-sea level, along with the beach ridge locations, were recorded, and used to develop a paleo-sea level curve.

There is inherent uncertainty in the GPR results. One source of uncertainty lies in converting the two-way-travel time in nanoseconds to depth in meters. A major factor contributing to this uncertainty is lack of knowledge of the actual water saturation of the sand. Radar velocity for saturated sand is 0.06 m/ns, while radar velocity in completely dry sand is

0.15 m/ns, and radar velocity for seawater is 0.01 m/ns. For this study, a radar velocity of 0.03 m/ns was used. By using a radar velocity equal to or greater than 0.06 m/ns, depth values obtained significantly greater than the regional sea-level curve created by Balsillie and Donoghue (2004). When using 0.06 m/ns, calculated depths are approximately 50% greater than when using 0.03 m/ns. Therefore it is important to account not only for the presence of water, but also for the fact that groundwater on a barrier island is likely to be brackish. Time-to-depth conversion using a constant velocity has also been used in a previous GPR study on a barrier island (Garrison et al., 2010). However, the actual value of radar velocity is not critical. The error in elevation associated with this calculated value is not important, because the purpose of this study was not to determine the true elevation of late Holocene sea level, but rather to chronicle the periods of rise and fall, which are the important climate signals.

There is also uncertainty introduced by the OSL dating method. By averaging the error for each of the five OSL dates used (Table 1), the mean error for the ages of the paleo-beach ridges is approximately 9.5%. This error applies to the ages along the x-axis of the sea level curve in Figure 26.

The paleo-sea level record obtained from the GPR transect was found to date from approximately 3500 BP to 1100 BP. The paleo-sea level curve records multiple oscillations in sea level during the nearly 2500-year record, with the most oscillations occurring between 2000 years BP and 1100 years BP. The subsurface depth values associated with each oscillation have some inherent error, due to uncertainty in knowing the true velocity of the radar pulse. However, they do represent a true trend of paleo-sea level (Fig. 26). Seventeen rise and fall trends have been identified in the GPR profile, and each rise and fall of sea level will be described from oldest to youngest (north to south).

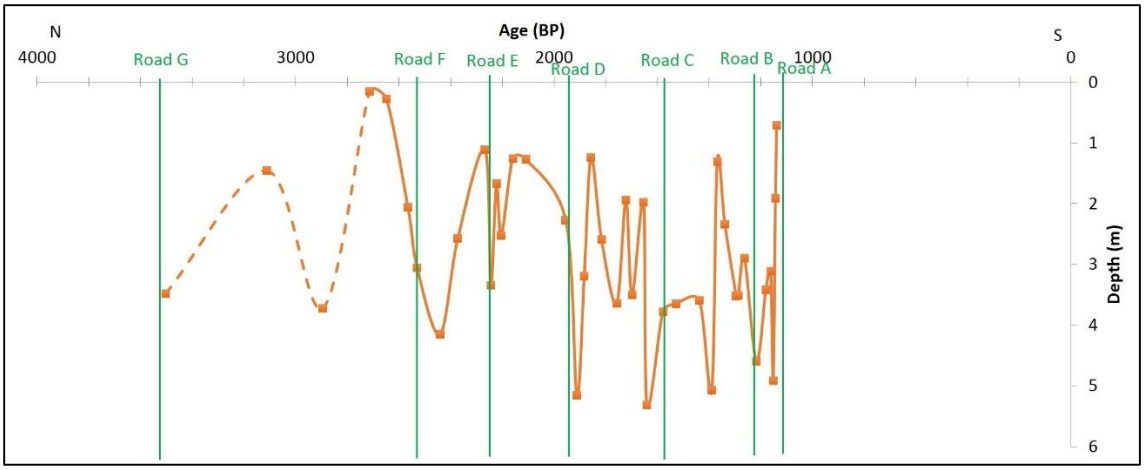

Fig. 26. Proxy sea level-curve, based on beach ridge basal elevations from St. Vincent Island ground-penetrating radar (GPR) transect. Ages are based on interpolation of optically stimulated luminescence (OSL) ages of beach ridge basal deposits. South is seaward direction. Dashed lines represent poor data quality. Location of Roads A through G (from Fig. 21) along the GPR transect are represented by the green vertical lines.

Beginning in the north of St. Vincent Island on Road 4, approximately 40 meters south of Road G (approximately 140 meters along the GPR transect data profile), the beach ridge paleo-sea level proxy history begins at approximately 3500 BP. From 3500 BP to 3100 BP, paleo-sea level rose. This paleo-beach ridge was located significantly higher in elevation than the paleo-beach ridge located at 3500 BP, and approximately 330 meters along the GPR transect. This rise in sea level may be correlated with the overall increase in precipitation and increase in ENSO events found in Moy et al. (2002) during the period from approximately 3500 yr BP to 3100 yr BP, and also may be correlated with the increase in storminess from 3500 yr BP to 3200 yr BP reported by Donnelly and Woodruff (2007). Following the sea level rise, the next paleo-beach ridge was located 430 meters along the transect. This proxy records a sea level fall from approximately 3100 BP to 2900 BP, with a magnitude similar to that of the sea level rise from approximately 3500 BP to 3100 BP. After sea level fell from approximately 3100 BP to 2900 BP, paleo-sea level rose from approximately 2900 BP to 2600 BP. The paleo-beach ridge indicating the rise in sea level is approximately 540 meters along the north to south transect. This is the highest magnitude paleo-sea level recorded in the paleo-sea level curve determined by the

GPR profile. This rise in sea level may correspond with an increase in warm ENSO events from 2700 yr BP to 2500 yr BP described in Moy et al.'s (2002) proxy study.

Following the highest paleo-sea level recorded, sea level then fell between approximately 2600 BP and 2400 BP. This regression is marked by a paleo-beach ridge located approximately 760 meters along the transect. This was the largest sea-level fall identified by the paleo-sea level curve, and of equal or greater magnitude to the rise in sea level from approximately 2900 BP to 2600 BP. This sea level fall may be correlated with a decrease in storminess from approximately 2500 yr BP to 2300 yr BP found by Donnelly and Woodruff (2007). Between approximately 2400 BP and 2300 BP, a rise in sea level was indicated by a paleo-beach ridge located approximately 960 meters along the transect. This rise in sea level has a magnitude similar to that of the sea-level rise from approximately 3500 BP to 3100 BP. Between 2300 BP and 2200 BP, sea level experienced several oscillations, but overall fell slightly. The paleo-beach ridge marking this slight fall in sea level was found approximately 1090 meters along the transect. An overall trend of a sea level rise can be observed from approximately 2400 BP to 2200 BP, which may be correlated with a period of greater storminess represented by an increase in grain size from 2300 yr BP to 2200 yr BP found by Donnelly and Woodruff (2007) and also an increase in ENSO events from 2300 yr BP to 2000 yr BP found by Moy et al. (2002).

After the slight fall in sea level, a much larger magnitude fall in sea level occurred between approximately 2200 BP and 1900 BP. The proxy indicator was located approximately 1390 meters along the transect. This fall in sea level is nearly the same magnitude of the sea-level fall which occurred from approximately 2600 BP and 2400 BP. A short lasting rise in sea level is then indicated by a paleo-beach ridge identified approximately 1460 meters south along the transect. This rise in sea level is nearly the same magnitude of the sea-level rise from approximately 2400 BP and 2300 BP. An increase in warm ENSO events from 1800 yr BP to around 1600 yr BP found by Moy et al. (2002) and an increase in the frequency of intense storms

from 1800 yr BP to 1700 yr BP found by Donnelly and Woodruff (2007) may be correlated with the sea level rise identified by the paleo-beach ridge located at approximately 1460 meters south along the transect. After approximately 1900 BP, sea level fell until approximately 1800 BP. This paleo-beach ridge is seen approximately 1580 meters south along the transect, and is one of the smaller falls in sea level. Between approximately 1800 BP and 1700 BP, sea level is seen to have several small oscillations in the nearly 100-year time period, but an overall rising trend is indicated by the paleo-beach ridge located 1710 meters along the transect. Sea level then fell for a short period of time.

One important observation is that shoreline sedimentation is episodic, and the deposition of large volumes of sediment can occur in very short time intervals (Garrison et al., 2010). After falling for several years, sea level then rose between approximately 1600 BP and 1400 BP. This is indicated by multiple paleo-beach ridges identified between 1600 BP and 1400 BP, and is one of the smaller rises in sea level. In this nearly 200-year time period, sea level rose from approximately 1600 BP to 1400 BP, beginning with a rapid rise, which slowed to a gradual rise nearing approximately 1400 years BP. The rapid rise is indicated by a paleo-beach ridge located approximately 1800 meters along the transect, and the gradual rise can then be seen by paleo-beach ridges at approximately 1500 BP and finally at 1400 BP. This overall rise in sea level from approximately 1600 BP to 1400 BP may be correlated with an increase in sea-surface temperature from 1500 yr BP to 1300 yr BP reported by Richey et al. (2007), an increase in the frequency of intense storms between 1600 yr BP to 1500 yr BP reported by Donnelly and Woodruff (2007), and an increase in ENSO events from 1500 yr BP to 1300 yr BP reported by Moy et al. (2002). Sea level fell for a short duration, indicated by a paleo-beach ridge located at approximately 2030 meters south along the GPR transect. This sea-level fall is of similar magnitude to the rise of sea level experienced from approximately 1600 BP and 1400 BP. Following this short fall in sea level, a short rise in sea level occurred. This sea level rise may be correlated with an increase in

the frequency of intense storms from 1300 yr BP and 1200 yr BP found by Donnelly and Woodruff (2007), and is of similar magnitude to the rise in sea level from 1900 BP to 1800 BP.

Between approximately 1400 BP and 1200 BP, an overall sea-level trend is seen to fall, with several small oscillations identified. The paleo-beach ridge indicating the overall fall in sea level is located approximately 2520 meters south along the transect. A decrease in sea-surface temperature from 1300 yr BP to 1200 yr BP found by Richey et al. (2007), a decrease in the frequency of intense storms identified by the decrease in grain size from 1300 yr BP to 1200 yr BP found by Donnelly and Woodruff (2007), and a decrease in ENSO events from 1300 yr BP to 1100 yr BP found by Moy et al. (2002) may all correspond with the fall in sea level from approximately 1400 BP to 1200 BP identified by the GPR data. The final sea-level rise, which is similar in magnitude to the sea level rise from 2900 BP to 2700 BP, indicated by the GPR transect is located 2590 meters along the transect. This rise in sea level occurred between approximately 1200 BP and 1100 BP and may be correlated to the rise in sea surface temperatures from 1200 yr BP to 1000 yr BP found by Richey et al. (2007) and an increase in the frequency of intense storms from 1100 years BP to 1000 years BP reported by Donnelly and Woodruff (2007).

4.2 Interpretation of Sediment Texture Data

After analyzing the sediment core textural data, a geological signature for paleo-storms in the long-term sediment record was identified, using a combination of sedimentological signatures and radiometric dating. These sedimentological signatures being increases in percent sand and mean grain size. Figure 27 shows an example of such a signature, from a similar coastal lake in a previous study in this region (Coor, 2012). The results of that study showed that periods of greater frequency of major storms are evidenced by anomalies (peaks in percent sand and mean

grain size) in the sediment texture data. Instead of showing single storm events, the peaks in the sediment data were said to represent time intervals of greater or lesser storm frequency (Coor, 2012). The sediment analysis in this study (Fig. 23) has a higher sampling resolution than the analysis shown in Figure 27. This is due to the use of the laser particle analyzer, rather than the sieving and settling tube methods employed in the study shown in Fig. 27.

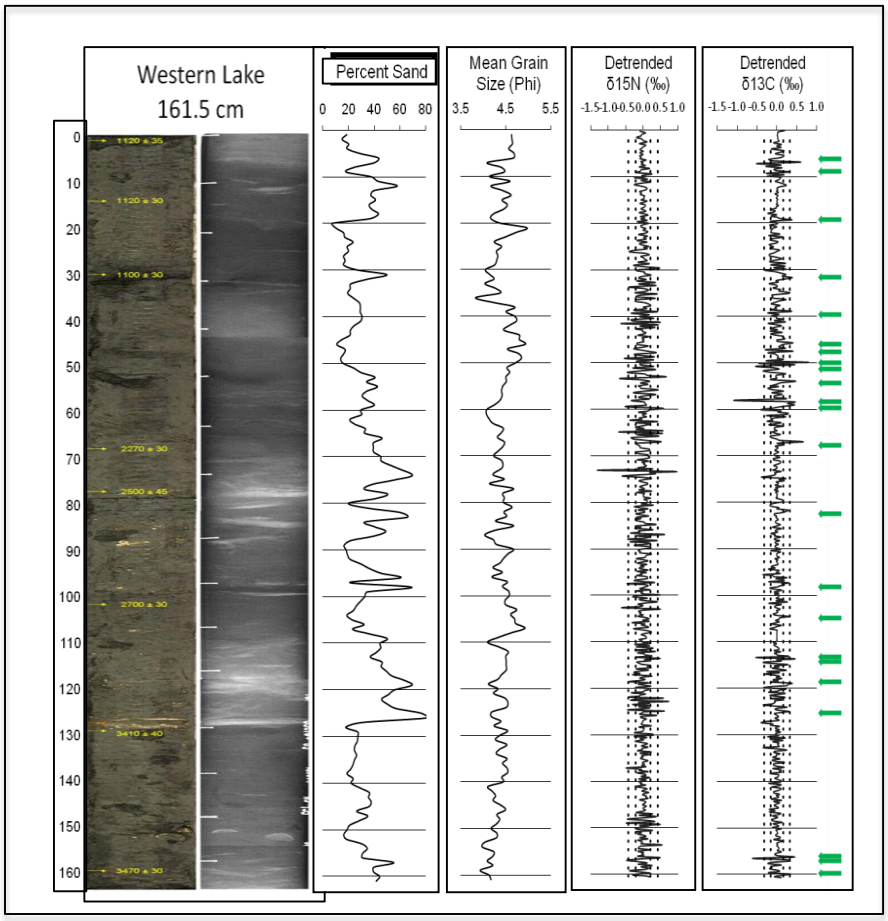

Fig. 27. Example of paleo-storm analysis of sediment core taken from Western Lake, on the NW Florida coast, approximately 100 km west of St. Vincent Island study area. In this case, the arrows on the far right indicate possible periods of greater storminess. Figure adapted from Coor (2012).

The upper 41.5 cm of the Oyster Pond core was analyzed to determine if the peaks in percent sand and mean grain size could be used to reflect the timing of known historic storm and

strong surge events. The storm surge history was obtained by analyzing the long-term tide gauge data from the NOAA station at Apalachicola, FL (Fig. 4) (NOAA, 2014a). A surge height that could influence the sediment in the pond in this case was determined to be one that is greater than +1.1 m (all events below the monthly tide gauge height maximum data for each year plus one half of a standard deviation) (Table 2). Anything less than 1.1 m would not be able to overtop the beach ridges seaward of the pond (fronting the pond) and contribute sediment to the pond. The tide gauge values corresponding to the different storm and surge events are likely less than water levels which actually occurred on St. Vincent Island, due to the tide gauge at Apalachicola, FL, being protected from storm wave run-up and surge in the Apalachicola River (Coor, 2012). Because of higher sedimentation rates in the upper 25 cm of the core, individual storm surge events can be discerned. Within the historic record of the sediment core (the upper 41.5 cm), these sediment texture anomalies can be correlated with known historic storm data. However, as sedimentation rates decrease with depth in the core, the larger peaks of increase in percent sand and increase in mean grain size likely represent longer periods of increased storminess. Decreases in percent sand and decreases in mean grain size (larger Ø size) represent periods of calm or less storminess.

Table 2. High-water events sufficient to affect Oyster Pond		
Event	**Date**	**Surge Height (m)**
Surge Event	9/2009	1.11
Hurricane Dennis	7/2005	2.22
Surge Event	9/2004	1.36
Surge Event	9/2002	1.15
Hurricane Earl	9/1998	1.57
Hurricane Opal	10/1995	1.74
Surge Event	10/1994	1.26
Hurricane Elena	9/1985	1.27
Hurricane Kate	11/1985	1.99
Hurricane Eloise	9/1975	1.27
Hurricane Agnes	6/1972	1.63
Unnamed Hurricane	1926	n/a
Unnamed Hurricane	1906	n/a
Unnamed Hurricane	1903	n/a
Unnamed Hurricane	1899	n/a

NOTE: Storm dates taken from the historic storm record (NOAA, 2014b). Events earlier than 1972 were not recorded at Apalachicola tide gauge station, and were obtained from the historic storm record (NOAA, 2014b) and SURGEDAT (Needham, 2011).

There are several sources of uncertainty in this storm model created from the core sediment data. One source of uncertainty arises from the age model. The core chronology is based on lead-210 analysis of the upper 41 cm of the core, along with one radiocarbon date in the lower part of the core. The radiocarbon date has an uncertainty of approximately 10%. This creates a vertical uncertainty in age. Another source of uncertainty is related to the sampling interval, every 0.5 cm. Each centimeter of core below 41 cm represents approximately 162 years, and so every 0.5 cm sample represents approximately 81 years. An additional amount of

uncertainty comes from the linear age-depth model being used for the ages of the samples below the last known lead-210 date. By assuming a constant sedimentation rate, which in actuality is likely not the case, an error of approximately +/-100 years arises from the uncertainty due to the age model and the sampling interval.

In order to correlate peaks in percent sand and mean grain size, a history of known storms was required. Using the NOAA Historical Tracks database (NOAA, 2014b), a list of storms that had passed within 140 km of Oyster Pond was compiled. The distance of 140 km was used to represent the mean radius to hurricane force winds for category 3 storms with wind speeds near 50 m/s (Keim et al., 2007). The paths of the historical hurricanes can be seen in Figure 28.

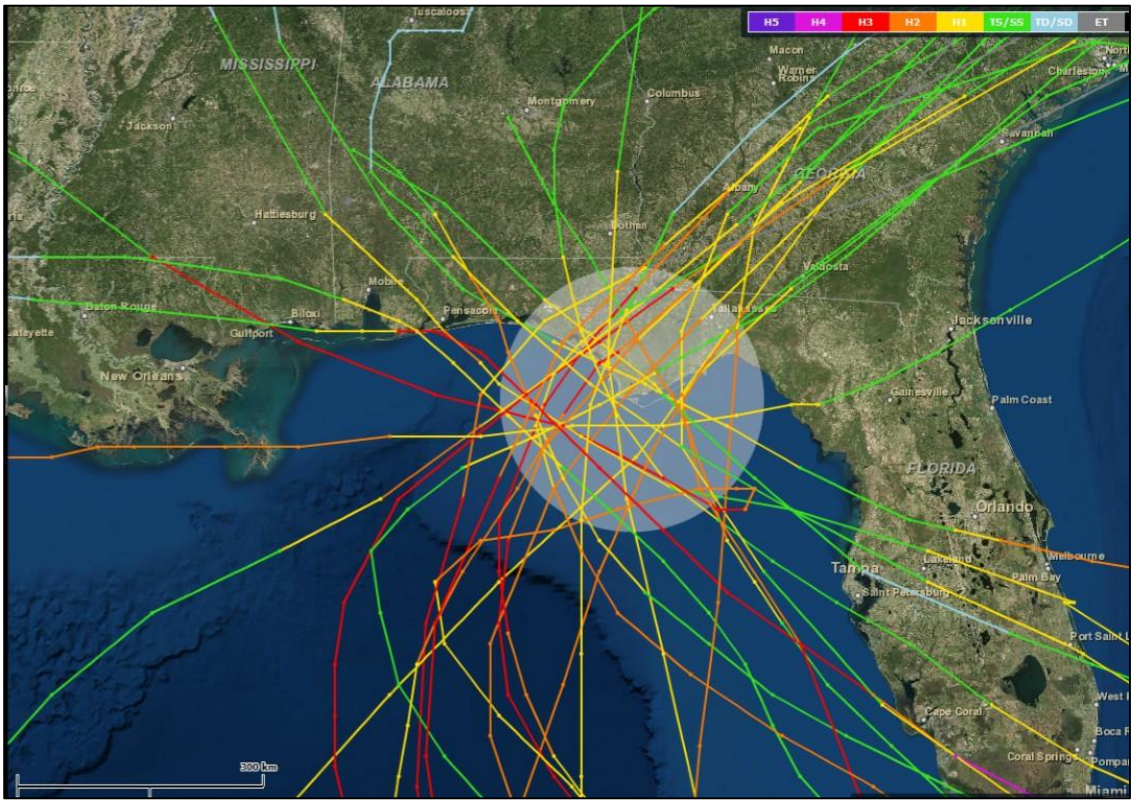

Fig. 28. Tracks of known historical hurricanes within 140 km of St. Vincent Island. Tracks include tropical storms (green lines), Category 1 hurricanes (yellow lines), Category 2 hurricanes (orange lines), and Category 3 (major) hurricanes (red lines) (NOAA, 2014b).

By analyzing the tide gauge data to determine storm surge height and hurricane data obtained from the NOAA Historical Tracks database, fifteen different known high water events were recorded from 1899 AD to 2009 AD (Table 2). The events listed in Table 2 after 1972 were determined using both the tide gauge data (NOAA, 2014a) and the historical storm track data (NOAA, 2014b), while the events prior to 1972 were determined using only the historical storm track data (NOAA, 2014b) . This time period is represented by the upper 39.5 cm of the core. These known events can be identified as peaks showing increase in percent sand and an increase in mean grain size (Figure 29). The peaks below 39.5 cm represent frequency of intense storms, not just single events. This is due to the time spans becoming compressed downcore due to compaction, and a likely increase in sedimentation rates in historic time. The sediment texture results will be described from top to bottom (youngest to oldest) as well as the peaks below 39.5 cm to the bottom of the core at 80.5 cm. In addition to the known events, several false positives can be identified within the upper 40 cm of the core as well as a potential false positive peak within the lower 40 cm. False positives may be a result of wind-driven waves or high water events of lesser magnitude that somehow inundated the lake, causing coarse sediment to enter. False positives are determined by peaks in percent sand and mean grain size not corresponding to known historic storms and surge events, or peaks being represented by only one data point. The entire 80.5 cm of the sediment core with identified storm events and periods of increased frequency of intense storms is shown in Figure 30.

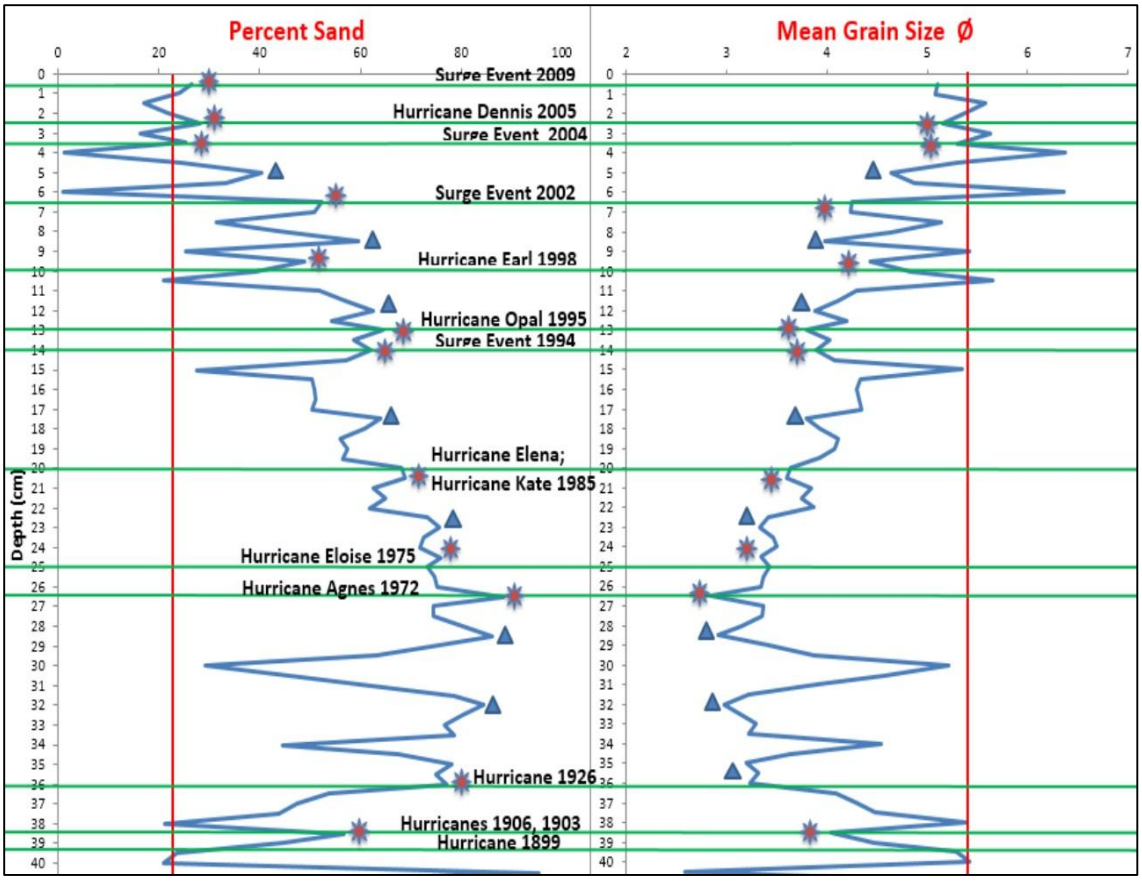

Fig. 29. Oyster Pond core 092710-01 partial sediment texture profiles, showing thirteen known historic storm and surge events (horizontal green lines) correlated with peaks in percent sand and mean grain size (red dots). Blue triangles indicate false positives. The vertical red lines represent additional criteria for developing the storm model. In order to be considered an event, the peaks must be greater that the red line.

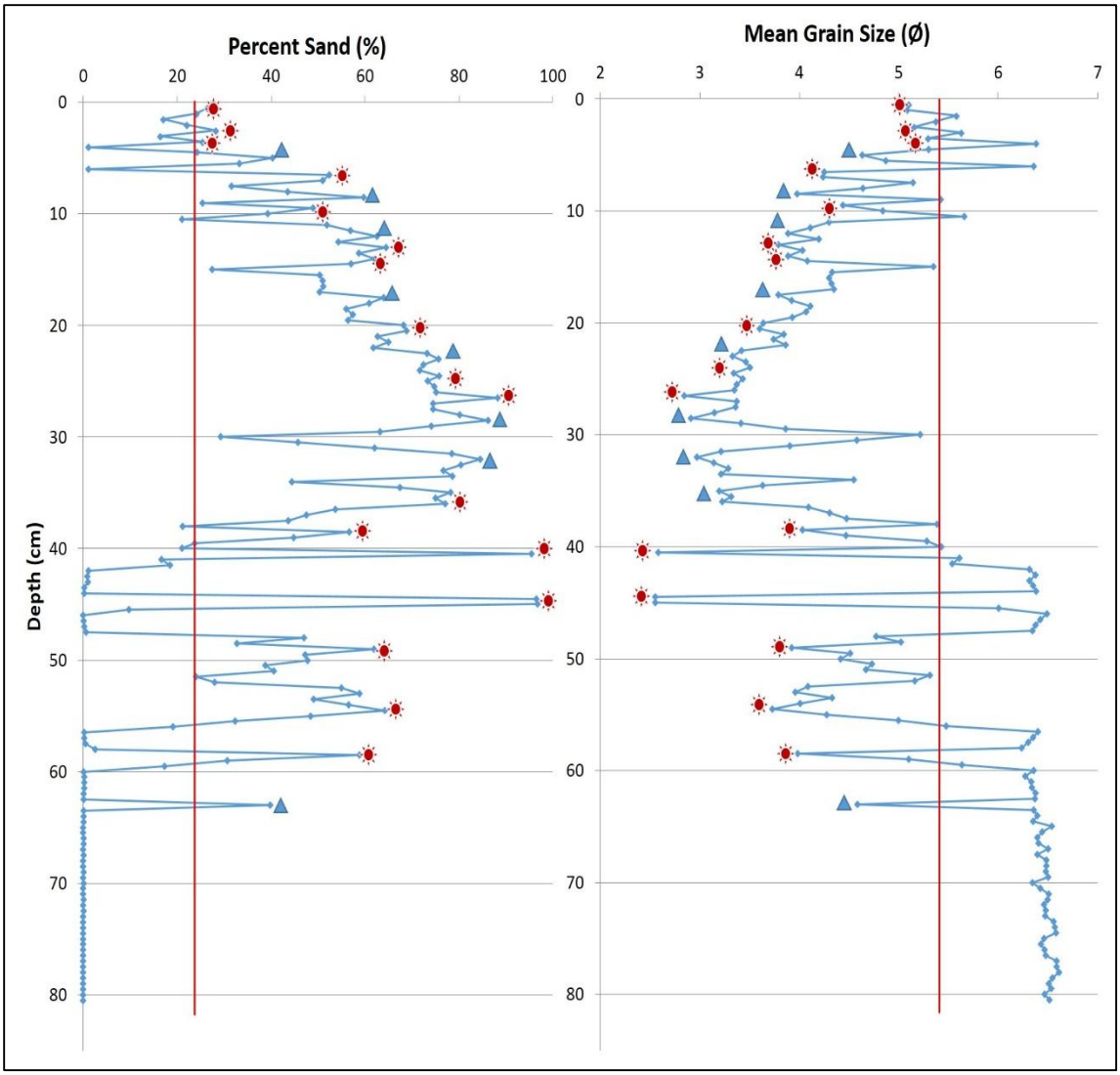

Fig. 30. Oyster Pond core 092710-01 full length percent sand and mean grain size profiles, the peaks indicating periods of greater frequency of intense storms (red dots), and false positives (blue triangles). The red vertical lines represent additional criteria for the storm model. In order to be considered an event, the peaks must be greater that the red line.

The uppermost peak at 0.5 cm depth represents an event with a +1.11 meter high tide event in November 2009. The second peak at 2.5 cm depth represents Hurricane Dennis in 2005, which was a category 4 hurricane and had a surge of +2.2 meters. The third peak at 3.5 cm depth represents a +1.36 meter high tide event in 2004. The first false positive appears at 5 cm depth. The definition of a false positive is described above in section 4.2. The peak at 6.5 cm represents

a storm surge event in 2002 with a +1.15 meter high tide. The top four identified events correspond to the increase of percent sand and the increase in mean grain size (lower phi size).

The next false positive is at 8.5 cm depth. The peak at 9.5 cm represents Hurricane Earl in 1998, which was a category one hurricane and caused a +1.57 meter storm surge. This event had a percent sand value of approximately 48.9% and a mean grain size of 4.4 Ø. The peak at 12 cm is interpreted as another false positive. Hurricane Opal in 1995 is represented by the peak at 13 cm. This event was a category three hurricane, caused a +1.74 meter storm surge, and had a percent sand value of approximately 64.5%. The peak at 14 cm depth represents a surge of +1.26 meters in 1994. This event has a percent sand value of 61.9% and a mean grain size of 3.8 Ø. This peak comes after a period of several years with few intense storms/surges. The peak located at 17.5 is another false positive.

The broad peak from 20 cm to 20.5 cm represents Hurricanes Elena and Kate, both occurring in 1985. Hurricane Elena was a category three hurricane with a +1.26 meter surge, and Hurricane Kate was a category two hurricane with a +1.99 meter surge. This event has a percent sand value of 68.8%. Hurricane Eloise (1975) is represented by the peak located at 25 cm. For this event, the sediment profile showed a percent sand of 75.8% and a mean grain size of 3.3 Ø. The next peak that corresponds to an event is located at 26.5 cm depth, representing Hurricane Agnes in 1972. This event was a category one hurricane with a +1.63 meter storm surge at the tide gauge in Apalachicola, FL, and had a percent sand value of approximately 88.2%. The next two peaks at 28.5 cm and 32 cm are designated as false positives, although they could potentially be high surge events not related to storms. The Apalachicola tide gauge provides a continuous record of water level only dating back to 1972. Prior to that, surge data are more regional and are sparse. The peak located at 36 cm represents an unnamed hurricane in 1926. This peak had a percent sand value of approximately 77.1% and a mean grain size of 3.2 Ø. This unnamed hurricane was a category three hurricane at the closest location to St. Vincent Island. The peak

located at 38.5 cm represents multiple years, thus being classified as a period of greater storminess. One unnamed storm, which occurred in 1906, was a category three hurricane, and an unnamed category one hurricane occurred in 1903. As previously mentioned, sedimentation rate diminishes downcore and these multiple storms are apparently represented by the peak at 38.5 cm. This period of storminess has a percent sand value of 56.6% and a mean grain size of 4 Ø. This peak may also be correlated with the increasing trend in SSTs and Mg/Ca in G. ruber for this time period, as described by Richey et al. (2007).

The peak at 40.5 cm appears to represent a period of greater storminess. Several category two and category one hurricanes were recorded for the period 1880 AD - 1900 AD (NOAA, 2014b). Regional tide surge data indicates surge events for the events prior to 1972 AD (Needham, 2011). The sediment record shows a percent sand value of 95.4% and a mean grain size of 2.5 Ø. The next peak is seen at 44.5 cm to 45 cm depth. This suggests that during the period of time between the peak at 40.5 cm and 44.5 cm, the barrier island underwent a period less storminess. This peak from 44.5 cm to 45 cm (approximately 1300 to 1200 AD) can be interpreted as a period with a greater frequency of storms. This period of higher frequency of storms may correspond with not only the increase in sea-surface salinity around 1200 AD reported by Nyberg et al. (2002), but also with an increase in sea-surface temperature at 600 yr BP reported by Richey et al. (2007), and a peak in warm ENSO events at 800 yr BP reported by Moy et al. (2002). The sediment record shows a percent sand value of 96% and a mean grain size of 2.5 Ø.

The next period of greater storminess is located at 49 cm, representing approximately 600 AD. This period of greater frequency of intense storms has a percent sand of 61.8% and a mean grain size of 3.9 Ø. This peak shows a period of increasingly greater frequency of intense storms before reaching the peak, and then followed by a period of lesser storminess. This peak at 49 cm may correspond with a peak in grain size at 1400 years BP reported by Donnelly and Woodruff

(2007), a peak in ENSO events at 1300 years BP reported by Moy et al. (2002), an increase in sea-surface temperatures at 1400 years BP reported by Richey et al. (2007), and a peak in sea-surface salinity around 700 AD reported by Nyberg et al. (2002). Similarly, the peak at 54.5 cm (approximately -250 AD) is preceded and followed by periods of less storminess. The peak at 54.5 cm represents another period of greater storminess, with a percent sand value of 64.2% and a mean grain size of 3.7 Ø. This peak may correlate with a peak in storminess at 2300 years BP reported by Donnelly and Woodruff (2007). The period of less storm frequency between the peak at 54.5 cm and the peak at 49 cm appears to be less pronounced than the period of lower storminess following the peak at 49 cm and the period following the peak at 44.5 cm to 45 cm. The peak at 58.5 cm (-900 AD) represents a brief period of lower storminess. The sediment profile shows a percent sand of 58.8% and a mean grain size of 3.9 Ø. This peak may correlate with a small peak in grain size around 2900 years BP reported by Donnelly and Woodruff (2007) and an increase in ENSO events at 2800 years BP reported by Moy et al. (2002).

The last peak at 63 cm has a percent sand value of 39.7% and a mean grain size of 4.5 Ø. This peak could possibly be representative of a period of greater frequency of intense storms, or because it is represented by only a single point, it could be represent a false positive. For the remainder of the core, from 63.5 cm to 80.5 cm, a percent sand of 0% was recorded. The mean grain size for this section of the core varies slightly, but remains between 6.3 Ø and 6.5 Ø. According to radiocarbon dating, the approximate age of the sediment at 62.5 cm is roughly 3500 years BP. This sediment is likely to have been derived from inner shelf, shoreface sediment. Estuarine sediments were flushed out of the estuary and onto the shoreface, much as they are today via the inlets at either end of the island. St. Vincent Island built out on this shoreface sediment, which may explain why the low percent sand was recorded.

Upon analyzing the sediment texture data, and identifying paleo-storm events, a proxy paleostorm history was created (Fig. 31). This paleostorm history proxy was created from a

partial profile of mean grain size and percent sand from Oyster Pond core 092710-01. Several periods of increased storminess are shown between 0 to 1000 years BP. Also evident are periods of increased storminess between 1000 years BP and 2000 years BP, as well as a period of increased storminess slightly before approximately 3000 years BP.

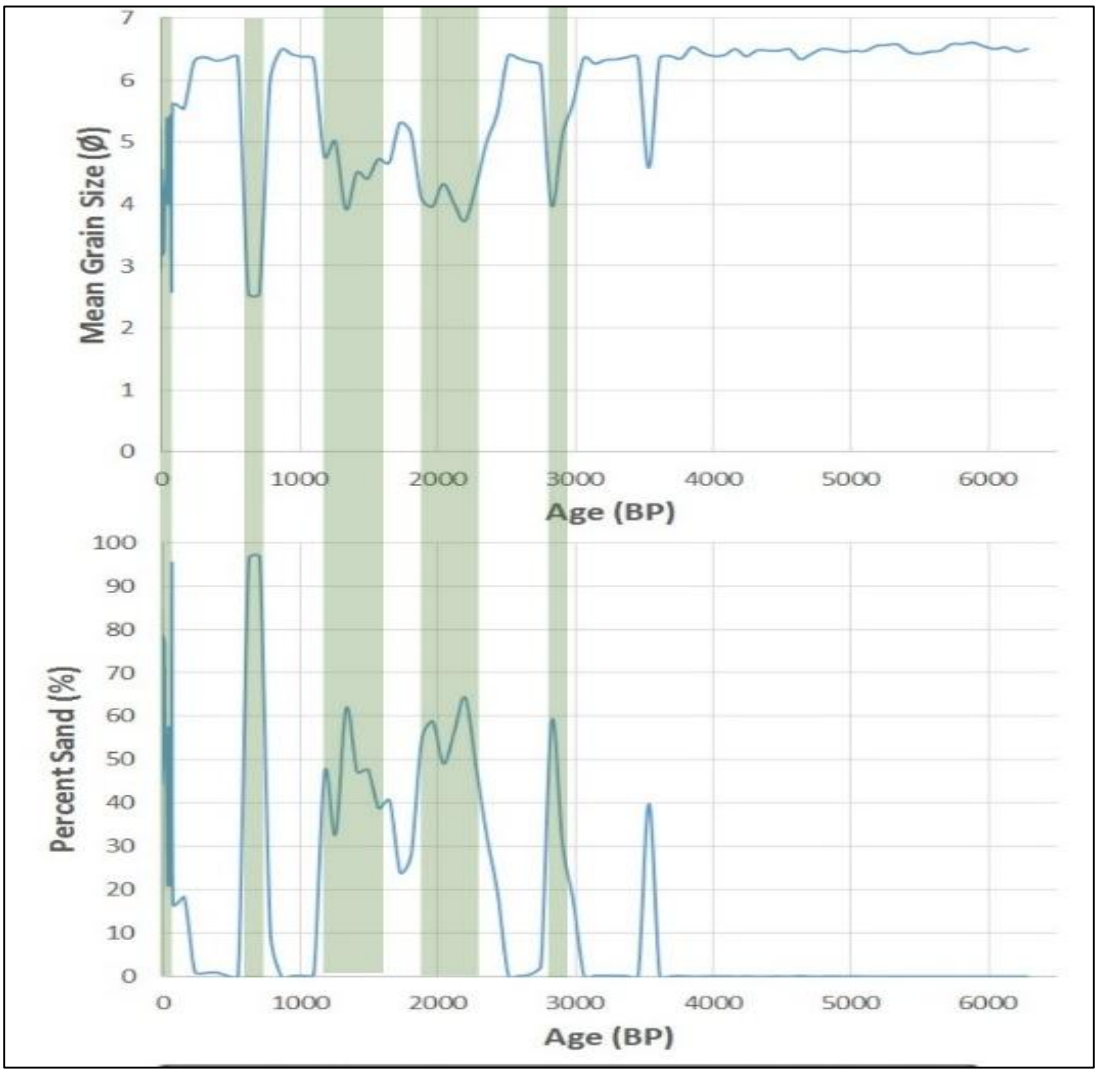

Fig. 31. Proxy paleostorm history created from partial profile of mean grain size and percent sand from core 092710-01. Green bars represent periods of increased storminess.

To help in better understanding the magnitude of the periods of storminess, an attempt was made to quantify storm surge during the identified stormy periods. To accomplish this, two

equations were employed. First, the settling velocity of the grains in the identified events had to be calculated. This was done by using the Gibbs equation (Komar, 1981; Fok-Pun and Komar, 1983):

$$W_S = [(1.33/C_d)((\rho_s - \rho)/\rho)gD]^{1/2}$$

where W_s is the settling velocity, C_d is the drag coefficient, ρ_s is the grain density of quartz, ρ is the density of water, g is the acceleration due to gravity, and D is the grain diameter.

After calculating the settling velocity, this value was then inserted into an equation calculating surge height (Woodruff et al., 2008):

$$H_b = \frac{(X_L^2 \, W_S^2)^{1/3}}{g^{1/3}}$$

where H_b is the surge height, X_L is the horizontal distance of storm transport for the sediment particles (the distance from Oyster Pond to the Gulf shore), W_s is the settling velocity, and g is the acceleration due to gravity. The storm surge calculations can be seen in Table 3. Nearly all of the calculated storm surge heights on St. Vincent Island (Table 3) are greater than the measured surge heights at the Apalachicola tide gauge station. The likely reason is the fact that the Apalachicola tide gauge is partially protected from storm wave run-up and surge in the Apalachicola River.

Table 3. Calculated storm surge heights for identified events.

Depth	Mean Grain size	Settling Velocity (W_s) using C_d=2	Storm deposits	Calculated Surge Height (H_h)	Approximate Storm Category (Saffir-Simpson Scale)	Measured Surge Height
cm	cm	m sec^{-1}		(m)		(m)
0.5	0.0029	0.02	Surge Event 2009	1.7	2	1.1
2.5	0.0028	0.02	H. Dennis 2005	1.7	2	2.2
3.5	0.0025	0.02	Surge Event 2004	1.6	1 to 2	1.4
6.5	0.0052	0.02	Surge Event 2002	2.1	2	1.2
9.5	0.0046	0.02	H. Earl 1998	2.0	2	1.6
13	0.0072	0.03	H. Opal 1995	2.3	2	1.7
14	0.0068	0.03	Surge Event 1994	2.3	2	1.3
20	0.0080	0.03	H. Elena/ Kate 1985	2.4	2	1.3/2.0
24.5	0.0099	0.03	H. Eloise 1975	2.6	2 to 3	1.3
26.5	0.0139	0.04	H. Agnes 1972	2.9	3	1.6
36	0.0107	0.03	Unnamed Hurricane 1926	2.7	3	n/a
38.5	0.0061	0.03	Unnamed Hurricanes 1906 and 1903	2.2	2	n/a
40.5	0.0167	0.04	EVENT A	3.1	3	
44.5	0.0170	0.04	EVENT B	3.1	3	
49	0.0066	0.03	EVENT C	2.3	2	
54.5	0.0075	0.03	EVENT D	2.4	2	
58.5	0.0063	0.03	EVENT E	2.2	2	

4.3 Comparison with Other Proxy Evidence

Several areas of agreement can be observed between the proxy paleostorm history created in this study (Fig. 32) and a palostorm study from Western Lake, NW Florida (Coor, 2012).

Western Lake is located approximately 100 miles to the west of Oyster Pond, also on the Florida panhandle coast. Both proxy studies indicate periods of increased storminess between 0 and 1000 years BP, as well as a period of increased storminess centered at approximately 2000 years BP.

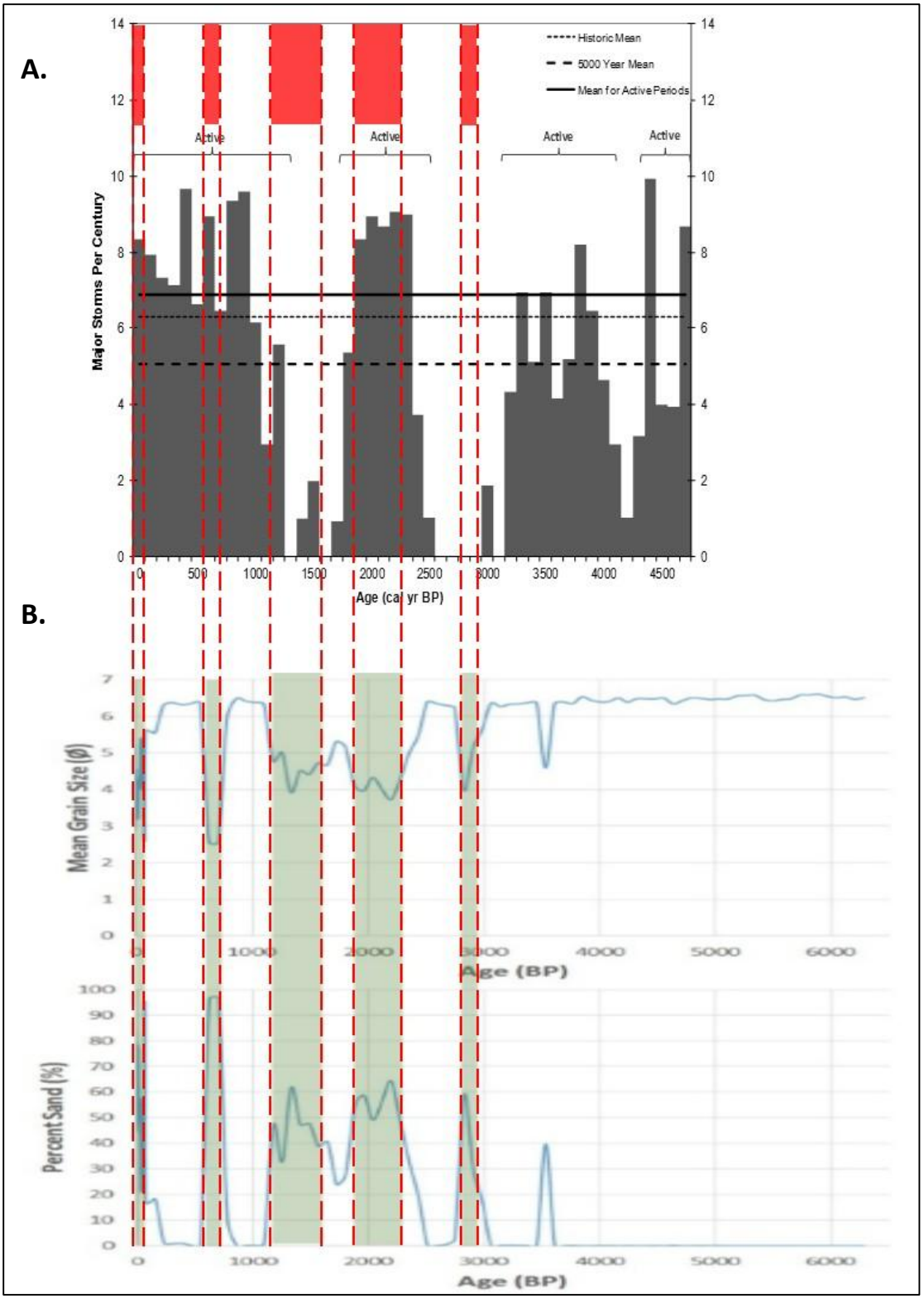

Fig. 32. Comparison of A.) Paleostorm study from Western Lake, NW Florida (Coor, 2012); B.) Proxy paleostorm history from Fig. 31 created from partial profile of mean grain size and percent sand from Oyster Pond core 092710-01. Red dashed lines and colored boxes indicate periods of increased storminess found in the Oyster Pond core.

Several components of the paleo-sea level proxy record and the paleo-storm proxy were found to correlate with a compilation other regional and global proxies compiled in Nott and Forsyth (2012) (Fig. 33). The paleostorm proxy data from the Texas coast (Wallace and Anderson, 2010), shows increased storminess from approximately 3500 BP to 1000 BP. Several increases in the frequency of intense storms obtained from the Oyster Pond sediment analysis, as well as increases in paleo-sea level obtained from the GPR transect occur within this time period. Similar to the storm proxy from Wallace and Anderson (2010), a storm proxy created by Liu and Fearn (1993, 2000) for the NW Florida and Alabama coast also indicates tropical cyclone activity from approximately 3500 BP to 1000 BP. During the approximately 1500-year period of increased storm activity reported by Liu and Fearn (1993, 2000), several periods of increased storm frequency can be seen in the sediment proxy record from Oyster Pond.

At approximately 3100 BP, the St. Vincent Island GPR data analysis indicates a rise in paleo-sea level, which also may be correlated to increased tropical cyclone activity identified by Lane et al. (2011) for a coastal sinkhole in NW Florida. At approximately 2800 BP, an increase in the frequency of intense storms is indicated by the sediment data analysis. This rise in paleo-sea level and increase in the frequency of intense storms can be correlated within a period of greater storm activity in the proxy created by Lane et al. (2011). At approximately 2700 BP, the GPR data analysis indicates a relatively large magnitude rise in paleo-sea level. At approximately 700 BP, the sediment data analysis indicates an increase in the frequency of intense storms, and may correlate with Lane et al.'s (2011) episode of greater storm activity during that time.

The paleostorm record in Nott and Forsyth (2012) does not indicate any systematic correlations for periods of storminess among the various paleostorm studies. However, there is one period centered around 3000 yr BP that indicates "global" storminess. That period of increased storminess is also recorded in the Oyster Pond sediments. The closest regional proxy

study (Lane et al. 2011) to Oyster Pond is in reasonably good agreement with the Oyster Pond record, especially in regard to the increased periods of storminess centered at about 3000 BP and 700 BP.

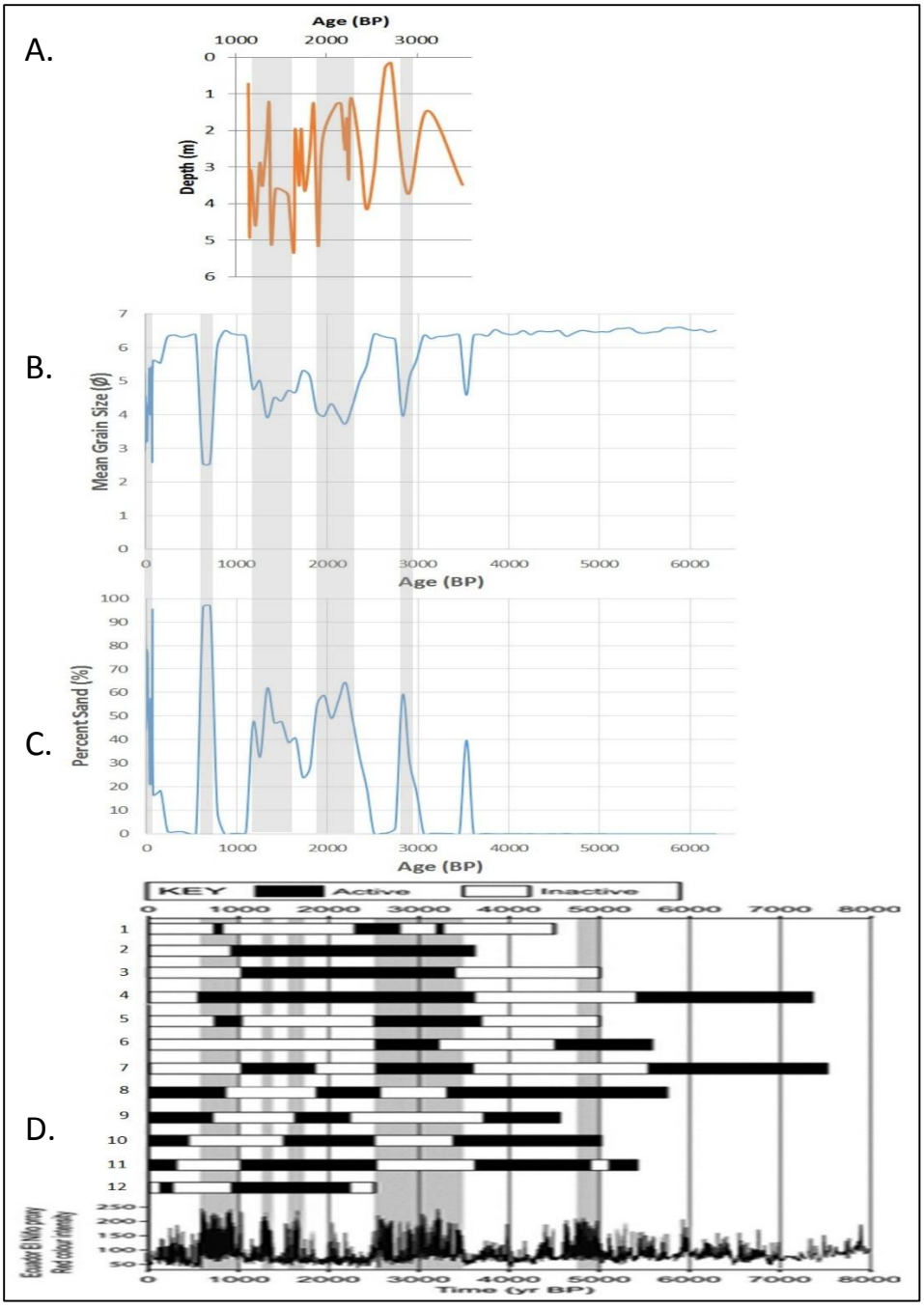

Fig. 33. Comparison of: (A) Proxy paleo-sea level curve created from GPR data from transect across St. Vincent Island; (B) and (C) Proxy paleostorm history created from sediment profile from Oyster Pond core 092710-01. Gray bars represent periods of increased storminess; (D) Summary of several regional and global proxy data studies showing periods of storm activity represented by the gray/black bars and inactivity represented by the white bars (adapted from Nott Forsyth, 2012). Sources indicated in (D) are: 1.= NW Florida 2 (Lane et al., 2011), 2= Texas (Wallace and Anderson, 2010), 3= Alabama/NW Florida (Liu and Fearn, 1993, 2000), 4= Western Australia (Nott, 2011), 5= Japan (Woodruff et al., 2009), 6= Belize (McCloskey and Keller, 2009), 7= Gulf of Carpentaria, Australia (Rhodes et al. 1980), 8= Cowley Beach, Australia (Nott et al., 2009), 9= Wonga Beach, Australia (Forsyth et al., 2012), 10= Rockingham Bay, Australia (Forsyth et al., 2010), 11= Puerto Rico (Woodruff et al., 2008b), 12= New York (Scileppi and Donnelly, 2007).

CHAPTER V

CONCLUSION

This study sought to improve the understanding of the effect climate has had on the frequency of intense storms, as well as sea-level change, in the northern Gulf of Mexico during the late Holocene. This investigation aimed to investigate climate proxies created from the northeastern Gulf of Mexico coast, and compare the outcome with additional regional climate proxies. This study also aimed to create a paleo-sea level proxy using GPR transect data from a beach-ridge plain.

The results yield two separate climate proxies for the Gulf of Mexico, one of which is unique to this study. Coastal barrier GPR data have not previously been used to develop a sea-level proxy. This paleo-sea level proxy correlates with previous climate proxies for the region. Multiple paleo-sea level rises and falls may be correlated with sea-surface temperatures in the Pigmy Basin in the northern Gulf of Mexico, the frequency of intense storms in Laguna Playa Grande, Vieques, Puerto Rico, changes in sea-surface salinities in the northeast Caribbean, and changes in precipitation and ENSO events in the southern Ecuadorian Andes.

The paleo-storm proxy obtained from the sediment core analysis is a new addition to regional paleo-storm history, and lends support to previous paleo-storm proxies for the region. Additionally, the paleo-storm proxy obtained in this study can be used to correlate periods of greater storm frequency with times of sea-level rise obtained from the GPR data gathered in this

study. This research has given an additional history of the frequency of intense storms recorded for the northern Gulf region, provided a new method of determining paleo-sea level, and helped correlate periods of greater storminess and sea-level change to climate change.

REFERENCES

Appleby, P., Oldfield, F., 1978. The calculation of lead-210 dates assuming a constant rate of supply of unsupported 210Pb to the sediment: *Catena*, v. 5, p. 15-18

Balsillie, J. H. and Donoghue, J. F., 2004. High resolution sea-level history for the Gulf of Mexico since the last glacial maximum: Florida Geological Survey Report of Investigations No. 103. Tallahassee, FL, Florida Geological Survey, 31 p.

Bender, M.A., Knutson, T.R., Tuleya, R.E., Sirutis, J.J., Vecchi, G.A., and Held, I.M., 2010. Modeled impact of anthropogenic warming on the frequency of intense Atlantic hurricanes: *Science*, v. 327, p. 454-458

CALIB, 2013. Stuiver, M., Reimer, P., Reimer, R. http://calib.qub.ac.uk/calib/calib.html (accessed 12/13/11).

Coor, J., 2012, Coastal Lake Paleoclimate Records: Late Quaternary Paleostorm Chronology for the Northeastern Gulf of Mexico Coast [Ph.D Thesis]: Tallahassee, Florida State University, 131 p.

Donnelly, J. P. and Woodruff, J. D., 2007. Intense hurricane activity over the past 5,000 years controlled by El Niño and the West African monsoon: *Nature*, v. 447, no. 7143, p. 465-468

Donoghue, J. F., 2011, Sea-level history of the northern Gulf of Mexico and sea-level rise scenarios for the near future: *Climatic Change*, v. 107, no. 1, p. 17-33.

Elsner, J.B., Kossin, J.P., and Jagger, T.H., 2008. The increasing intensity of the strongest tropical cyclones: *Nature*, v. 455, p. 92-95.

Esper, J., Cook, E.R. and Fritz, H.S., 2002. Low-Frequency Signals in Long Tree-Ring Chronologies for Reconstructing Past Temperature Variability: *Science*, v. 295, no. 5563, p. 2250-2253

Fairbanks, R.G., 1989. A 17,000-year glacio-eustatic sea level record: influence of glacial melting rates on the Younger Dryas even and deep ocean circulation: *Nature*, v. 342, p. 637-642

Fairbridge, R.W., 1961, Eustatic changes in sea level: In: Physics and Chemistry of the Earth. Eds. L.H. Ahrens, Frank Press, Kalervo Rankiama, S.K. Runcorn. V.4, p. 99-185.

Fisher, S. C., Stewart, R. R., Jolt, H. M., 1992. Processing ground penetrating radar (GPR) data: Consortium for Research in Elastic Wave Exploration Technology (CREWES) Research Report 1992, v. 4, ch. 11, p. 11-1 – 11-22

Fok-Pun, L., and Komar, P.D., 1983. Settling velocities of planktonic foraminifera: Density variations and shape effects: *Journal of Foraminiferal Research*, v. 13, p. 60-68.

Folk, R. L., 1974. Petrology of Sedimentary Rocks: Austin, TX, Hemphill Publ., 182 p.

Forrest, B.M., 2007, Evolution of the Beach Ridge Strandplain on St. Vincent Island, Florida [Ph.D. Thesis]: Tallahassee, Florida State University, 288 p.

Forsyth, A., Nott, J., and Bateman, M., 2010. Beach ridge plain evidence of a variable late-Holocene tropical cyclone climate, North Queensland, Australia: *Palaeogeogr. Palaeoclimatol. Palaeoecol.*, v. 297, p. 707-716, doi: 10.1016/j.palaeo.2010.09.024

Forsyth, A., Nott, J., Bateman, M.D., and Beaman, R.J., 2012. Juxtaposed beach ridges and foredunes within a ridge plain- Wonga Beach, northeast Australia: *Marine Geology*, 307-310, 111-116, doi: 10.1016/j.margeo.2012.02.012

Foster, E.R., Sprugeon, D.L., and Cheng, J., 2000. Shoreline change rate estimates, Walton County: *Florida Department of Environmental Protection*, Report No. BCS-2000-02k, p. 59

Garrison, J.R., Jr, Williams, J., Miller, S.P., Weber, E.T. II, McMechan, G., and Zeng, X., 2010. Ground penetrating radar study of North Padre Island: Implications for barrier island internal architecture, model for growth of progradational microtidal barrier islands, and Gulf of Mexico sea-level cyclicity: *Journal of Sedimentary Research*, v. 80, p. 303-319, doi: 10.2110/jsr.2010.034

Grinsted, A., Moore, J.C., and Jevrejeva, S. 2009. Reconstructing sea-level from paleo and projected temperatures 200 to 2100 AD: *Climate Dynamics*, doi:10.1007/s00382-00008-00507-00382

Keim, B.D., Muller, R.A., and Stone, G.W., 2007. Spatiotemporal patterns and return periods of tropical storm and hurricane strikes from Texas to Maine: *Journal of Climate*, v. 20, p. 3498-3509

Kerr, R.A., 2001. A variable sun and the Maya collapse. *Science*, v. 292, n. 5520, p. 1293-1296.

Knutson, T.R., McBride, J.L., Chan, J., Emmanuel, K., Holland, G., Landsea, C., Held, I., Kossin, J.P., Srivastava, A.K., Sugi, M., 2010. Tropical cyclones and climate change: *Nature Geoscience*, v. 3, p. 157-163.

Komar, P.D., 1981. The applicability of the Gibbs equation for grain settling velocities to conditions other than quartz grains in water: *Journal of Sedimentary Petrology*, v. 51, p. 1125-1132.

Lane, P., Donnelly, J.P., Woodruff, J.D., and Hawkes, A.D., 2011. A decadally-resolved paleohurricane record archived in the late Holocene sediments of a Florida sinkhole: *Marine Geology*, v. 287, p. 14-30, doi: 10.1016/j.margeo.2011.07.001

Liu, K.B., and Fearn, M.L., 1993. Lake sediment record of late Holocene hurricane activities from coastal Alabama: *Geology*, v. 21, p. 793-796, doi: 10.1130/0091-7613(1993)021<0793:LSROLH>qres2000.2166

Liu, K.B., and Fearn, M. L., 2000. Reconstruction of prehistoric landfall frequencies of catastrophic hurricanes in northwestern Florida from lake sediment records: *Quaternary Research*, v. 54, p. 238-245

Marcott, S.A., Shakun, J.D., Clark, P.U. and Mix, A.C., 2013. A Reconstruction of Regional and Global Temperature for the Past 11,300 Years: *Science*, v. 339, no. 1198 p. 1198-1201

McCarthy, J.J., 2009. Reflections on: Our Planet and its life, origins, and futures: *Science*, v. 326, p. 1646-1655.

McCloskey, T.A., and Keller, G., 2009. 5000 year sedimentary record of hurricane strikes on the central coast of Belize: *Quat. Int.*, v. 195, p. 53-68, doi: 10.1016/j.quaint.2008.03.003

Moy, C.M., Seltzer, G.O., Rodbell, D.T. and Anderson, D.M., 2002. Variability of El Niño/Southern Oscillation activity at millennial timescales during the Holocene epoch: *Letters to Nature*, v. 420, no. 6912, p. 162-165

Neal, A., 2004. Ground penetrating radar and its use in sedimentology: principles, problems and progress: *Earth-Science Reviews*, v. 66, p. 261

Neal, A., Pontee, N. I., Pye, K., and Richards, J., 2002. Internal structure of mixed sand-and-gravel beach deposits revealed using ground-penetrating radar: *Sedimentology*, v.49, p. 789-804

Needham, H., 2011. SURGEDAT: The world's most comprehensive storm surge database: Southern Climate Impact Planning Program. http://surge.srcc.lsu.edu/data.html#SuperSurgeDat (accessed October 2014)

NOAA, 2014a. Tides and Currents. National Oceanic and Atmospheric Administration. National Ocean Service. http://tidesandcurrents.noaa.gov/sltrends/ (accessed August 2014)

NOAA, 2014b. National Oceanic and Atmospheric Administration. Historical Hurricane Tracks. http://csc.noaa.gov/hurricanes/# (accessed August 2014)

Nott, J., 2011. A 6,000 record of tropical cyclones from Western Australia: *Quat. Sci. Rev.*, v. 30, p. 713-722, doi: 10.1016/j.quascirev.2010.12.004

Nott, J., and Forsyth, A., 2012. Punctuated global tropical cyclone activity over the past 5.000 years: *Geophysical Research Letters*, v. 39, L14703, doi: 10.1029/2012GL052236

Nott, J., Smithers, S., Walsh, K., and Rhodes, E., 2009. Sand beach ridges record 6000 year history of extreme tropical cyclone activity in northeastern Australia: *Quat. Sci. Rev.*, v. 28, p. 1511-1520, doi: 10.1016/j.quascirev.2009.02.014

Nyberg, J., Malmgre, B.A., Kuijpers, A. and Winter, A., 2002. A centennial-scale variability of tropical North Atlantic surface hydrography during the late Holocene: *Palaeogeography, Palaeoclimatology, Palaeoecology*, v. 183, p. 25-41

Rhodes, E.G., Polach, H.A., Thom, B.G., and Wilson, S.R., 1980. Age structure of Holocene coastal sediments, Gulf of Carpentaria, Australia: *Radiocarbon*, v. 22, p. 718-727

Richey, J.N., Poore, R.Z., Flower, B.P. and Quinn, T.M., 2007. 1400 yr multiproxy record of climate variability from the northern Gulf of Mexico: *Geology*, v. 35, p. 423-426

Scileppi, E., and Donnelly, J.P., 2007. Sedimentary evidence of hurricane strikes in western Long Island, New York: *Geohem. Geophys. Geosyst.*, v. 8, Q06011, doi: 10.1130/G30729.1

Shepard, F.P., 1963. Thirty-five thousand years of sea level: In: Essays in Marine Geology in Honor of K.O. Emery. University of Southern California Press, Los Angeles, p. 1-10.

Shepard, F.P., 1964. Sea level changes in the past 6000 years, possible archaeological significance: *Science*, v. 143, p. 574-576.

Stapor, F.W., 1975. Holocene beach ridge plain development, northwest Florida: *Zeitschrift fur Geomorphologie*, Suppl. Bd. 22, p. 116-144

Stapor, F.W., Mathews, T.D., and F.E. Lindfors-Kearns, 1991. Barrier-island progradation and sea-level history in southwest Florida: *Journal of Coastal Research*, v. 7, n.3, p. 815-838.

Stapor, F.W., and Stone, G.W., 2004. A new depositional model for the buried 4000 yr BP New Orleans barrier: implications for sea-level fluctuations and onshore transport from nearshore shelf source: *Marine Geology*, v. 204, p. 215-234

Stone, G.W., and Penland, S., 1992. Historic shoreline change along the northern Gulf of Mexico: p. 267-279 in Majumadar, S.K., et al., eds., Natural and Technological Disasters: Causes, Effects and Preventive Measure; Philadelphia, Pennsylvania Academy of Science.

Stone, G.W. and Stapor, F. W., 1996. A nearshore sediment transport model for the Northeast Gulf of Mexico Coast: *Journal of Coastal Research*, v. 12, p. 786-792

Tanner, W.F., 1991. The Gulf of Mexico late Holocene sea level curve and river delta history: *Gulf Coast Association of Geological Societies, Transactions*, v. 41, p. 583-589

Tanner, W.F., 1992. Late Holocene sea-level changes from grain-size data: evidence from the Gulf of Mexico: *The Holocene*, v. 2, p. 249-254

Vecchi, G. A. and Knutson, T. R., 2008. On Estimates of Historical North Atlantic Tropical Cyclone Activity: *Journal of Climate*, v. 21, p. 3580-3600

Walker, K., Stapor, F. and Marquardt, W., 1995. Archaeological evidence for a 1750-1450 BP higher-than-present sea level along Florida's Gulf Coast: *Journal of Coastal Research Special No. 17*, p. 205-218

Wallace, D.J., and Anderson, J.B, 2010. Evidence of similar probability of intense hurricane strikes for the Gulf of Mexico over the late Holocene: *Geology*, v. 38, p. 511-514, doi: 10.1130/G30729.1

Woodruff, J. D., Donnelly, J. P., Emanuel, K., and Lane, P., 2008a. Assessing sedimentary records of paleohurricane activity using modeled hurricane climatology: *Geochemistry Geophysics Geosystems*, v. 9, no. 9, p. 1-12

Woodruff, J.D., Donnelly, J.P., Mohrig, D., and Geyer, W.R., 2008b. Reconstructing relative flooding intensities responsible for hurricane induced deposits from Laguna Playa Grande, Vieques, Puerto Rico: *Geology*, v. 36, p. 391-394, doi: 10.1130/G24731A.1

Woodruff, J.D., Donnelly, J.P., and Okusu, A., 2009. Exploring typhoon variability over the mid-to-late Holocene: Evidence of extreme coastal flooding from Kamikoshiki, Japan: *Quat. Sci. Rev.*, v. 28, p. 1774-1785, doi: 10.1016/j.quascirev.2009.02.005

APPENDIX

Sediment Data for core 092710-01

(Note: Each sample represents an average of two replicate analyses from the Cilas 1180 laser particle analyzer.)

Real Depth (cm)	Sample Number	% Sand	% Clay	% Silt	Moment Mean Grain Size (Ø)	Moment Standard Deviation for Mean Grain (Ø units)	Moment Skewness	Diameter at 5% (µm)	Diameter at 7% (µm)
0.5	1	26.44	8.16	65.40	5.10	1.95	-0.04	2.89	3.50
1	2	24.13	8.89	66.98	5.09	1.90	0.12	2.65	3.25
1.5	3	17.07	11.46	71.47	5.58	1.87	-0.21	2.36	2.83
2	4	22.00	10.70	67.30	5.37	1.96	-0.12	2.48	2.96
2.5	5	28.29	10.74	60.97	5.16	2.10	0.00	2.47	2.94
3	6	16.39	12.40	71.21	5.63	1.89	-0.20	2.30	2.73
3.5	7	25.37	11.70	62.92	5.29	2.06	-0.04	2.31	2.78
4	8	1.13	14.99	83.88	6.38	1.27	0.78	2.07	2.51
4.5	9	24.23	11.22	64.54	5.30	2.02	-0.08	2.41	2.88
5	10	40.29	8.96	50.75	4.63	2.16	0.34	2.69	3.26
5.5	11	33.23	10.64	56.13	4.87	2.14	0.27	2.37	2.87
6	12	1.06	15.19	83.75	6.36	1.27	0.85	2.00	2.44
6.5	13	52.34	8.50	39.16	4.25	2.22	0.65	2.76	3.37
7	14	50.99	7.58	41.43	4.24	2.15	0.64	2.95	3.66
7.5	15	31.52	11.51	56.97	5.15	2.20	-0.02	2.46	2.89
8	16	43.47	10.31	46.22	4.64	2.27	0.37	2.55	3.04
8.5	17	59.71	7.88	32.41	3.98	2.19	0.90	2.86	3.55
9	18	25.43	19.00	55.57	5.42	2.30	0.09	1.05	2.01
9.5	19	48.97	12.97	38.07	4.44	2.37	0.65	2.09	2.58
10	20	39.27	15.79	44.94	4.84	2.39	0.42	1.27	2.30
10.5	21	20.97	18.93	60.10	5.66	2.23	-0.16	0.93	2.03
11	22	51.86	11.06	37.08	4.30	2.31	0.72	2.38	2.86
11.5	23	56.91	10.18	32.91	4.11	2.30	0.85	2.48	2.99
12	24	62.51	8.72	28.77	3.89	2.22	1.03	2.68	3.29
12.5	25	54.33	9.12	36.54	4.20	2.25	0.73	2.66	3.23
13	26	64.53	8.07	27.40	3.79	2.17	1.12	2.80	3.49
13.5	27	58.65	9.25	32.11	4.03	2.26	0.90	2.62	3.17
14	28	61.99	8.92	29.09	3.89	2.21	1.06	2.63	3.23
14.5	29	57.08	10.01	32.91	4.08	2.26	0.91	2.50	3.02
15	30	27.45	17.66	54.89	5.35	2.32	0.06	1.15	2.20
15.5	31	50.36	11.87	37.77	4.33	2.32	0.73	2.24	2.71
16	32	50.98	11.39	37.63	4.30	2.29	0.76	2.32	2.79
16.5	33	51.07	11.25	37.68	4.32	2.31	0.70	2.40	2.85
17	34	50.37	11.61	38.01	4.35	2.31	0.70	2.32	2.78
17.5	35	63.92	8.32	27.76	3.79	2.13	1.19	2.75	3.40
18	36	60.89	9.11	30.00	3.93	2.20	1.04	2.64	3.20
18.5	37	56.03	10.44	33.53	4.11	2.27	0.90	2.43	2.92

Real Depth (cm)	Sample Number	% Sand	% Clay	% Silt	Moment Mean Grain Size (Ø)	Moment Standard Deviation for Mean Grain (Ø units)	Moment Skewness	Diameter at 5% (µm)	Diameter at 7% (µm)
19	38	57.40	9.77	32.82	4.07	2.26	0.90	2.55	3.07
19.5	39	56.42	9.65	33.93	3.93	2.19	1.01	2.63	3.23
20	40	68.19	7.21	24.60	3.64	2.09	1.30	3.04	3.90
20.5	41	68.90	6.96	24.14	3.60	2.03	1.39	3.15	4.14
21	42	62.62	8.23	29.15	3.85	2.15	1.10	2.81	3.51
21.5	43	65.06	7.43	27.51	3.74	2.09	1.21	2.95	3.71
22	44	61.81	7.90	30.29	3.87	2.11	1.11	2.94	3.74
22.5	45	73.21	5.65	21.15	3.42	1.89	1.62	3.72	5.20
23	46	75.68	5.27	19.05	3.33	1.88	1.70	3.73	5.21
23.5	47	72.43	5.89	21.67	3.46	1.96	1.51	3.41	4.58
24	48	71.72	6.22	22.06	3.50	2.03	1.42	3.30	4.38
24.5	49	75.82	5.28	18.90	3.34	1.94	1.61	3.72	5.17
25	50	73.33	5.56	21.11	3.43	1.96	1.51	3.60	4.93
25.5	51	74.74	5.21	20.05	3.37	1.90	1.61	3.79	5.25
26	52	75.17	5.06	19.78	3.35	1.85	1.69	3.96	5.57
26.5	53	88.25	2.35	9.40	2.84	1.36	2.80	19.49	34.17
27	54	74.48	4.93	20.58	3.37	1.88	1.60	3.95	5.54
27.5	55	74.51	4.76	20.74	3.36	1.82	1.66	4.12	5.89
28	56	80.20	3.90	15.91	3.15	1.73	1.94	5.16	7.64
28.5	57	86.23	2.59	11.19	2.91	1.43	2.57	10.95	22.77
29	58	74.07	4.41	21.52	3.41	1.99	1.35	4.32	5.91
29.5	59	63.20	6.05	30.75	3.86	2.16	0.89	3.43	4.44
30	60	29.30	10.78	59.92	5.21	2.15	-0.11	2.45	2.95
30.5	61	45.69	8.31	45.99	4.58	2.26	0.31	2.86	3.46
31	62	62.00	6.48	31.51	3.90	2.18	0.88	3.23	4.14
31.5	63	78.54	3.95	17.51	3.22	1.83	1.70	4.88	6.96
32	64	84.53	3.03	12.45	2.97	1.64	2.15	6.63	9.70
32.5	65	80.38	3.82	15.80	3.14	1.76	1.89	5.19	7.57
33	66	76.68	4.26	19.06	3.29	1.86	1.63	4.66	6.57
33.5	67	78.56	4.05	17.39	3.22	1.83	1.72	4.73	6.73
34	68	44.46	9.75	45.79	4.55	2.24	0.46	2.56	3.08
34.5	69	67.49	5.66	26.85	3.63	2.02	1.22	3.54	4.65
35	70	78.23	3.87	17.90	3.20	1.74	1.86	5.21	7.88
35.5	71	75.00	4.16	20.84	3.32	1.81	1.67	4.96	7.27
36	72	77.13	3.67	19.20	3.23	1.75	1.76	5.64	8.27
36.5	73	53.71	6.76	39.53	4.09	2.08	0.81	3.06	4.03
37	74	47.53	7.65	44.82	4.31	2.09	0.66	2.85	3.63

Real Depth (cm)	Sample Number	% Sand	% Clay	% Silt	Moment Mean Grain Size (Ø)	Moment Standard Deviation for Mean Grain (Ø units)	Moment Skewness	Diameter at 5% (µm)	Diameter at 7% (µm)
37.5	75	43.70	8.72	47.57	4.48	2.13	0.55	2.64	3.26
38	76	21.10	12.87	66.02	5.39	1.99	0.09	2.13	2.61
38.5	77	56.68	7.40	35.92	4.04	2.13	0.87	2.91	3.71
39	78	44.86	8.87	46.28	4.47	2.15	0.54	2.64	3.25
39.5	79	23.69	12.43	63.89	5.28	2.02	0.12	2.24	2.70
40	80	21.05	13.52	65.44	5.43	2.02	0.04	2.10	2.58
40.5	81	95.48	0.85	3.67	2.58	0.87	3.92	70.02	96.13
41	82	16.60	10.84	72.56	5.61	1.84	-0.33	2.55	3.00
41.5	83	18.40	10.10	71.50	5.54	1.87	-0.34	2.67	3.14
42	84	1.11	11.74	87.15	6.31	1.15	0.69	2.52	2.93
42.5	85	0.81	12.92	86.26	6.37	1.15	0.77	2.39	2.77
43	86	0.92	12.21	86.87	6.32	1.16	0.78	2.44	2.85
43.5	87	0.15	13.17	86.68	6.35	1.16	0.98	2.30	2.70
44	88	0.15	12.75	87.10	6.38	1.12	0.96	2.35	2.76
44.5	89	96.48	0.80	2.72	2.55	0.80	4.37	92.98	107.64
45	90	96.76	0.79	2.44	2.55	0.78	4.49	95.74	108.51
45.5	91	9.70	12.13	78.17	6.00	1.53	0.28	2.42	2.86
46	92	0.00	12.78	87.22	6.49	1.02	1.15	2.37	2.78
46.5	93	0.13	13.25	86.62	6.42	1.11	0.96	2.37	2.75
47	94	0.15	12.55	87.30	6.38	1.11	0.94	2.40	2.81
47.5	95	0.55	12.31	87.14	6.34	1.13	0.83	2.45	2.85
48	96	47.04	5.94	47.03	4.42	2.12	0.32	3.47	4.36
48.5	97	32.74	8.34	58.92	5.02	2.10	-0.09	2.91	3.47
49	98	61.86	5.04	33.10	3.92	2.10	0.77	4.08	5.19
49.5	99	47.24	6.77	46.00	4.51	2.21	0.25	3.24	3.98
50	100	47.72	6.74	45.55	4.41	2.15	0.39	3.26	4.00
50.5	101	38.80	7.70	53.50	4.73	2.13	0.15	3.03	3.65
51	102	40.57	7.84	51.59	4.67	2.15	0.22	3.02	3.62
51.5	103	23.95	9.82	66.23	5.31	1.98	-0.20	2.73	3.20
52	104	27.91	8.92	63.17	5.16	2.01	-0.15	2.85	3.37
52.5	105	54.94	5.41	39.65	4.09	2.08	0.65	3.72	4.66
53	106	58.88	6.05	35.06	3.96	2.09	0.84	3.56	4.50
53.5	107	49.09	6.09	44.83	4.33	2.11	0.45	3.44	4.27
54	108	56.53	5.04	38.42	4.01	2.05	0.72	3.87	4.92
54.5	109	64.24	4.21	31.55	3.73	1.94	1.03	4.43	5.79
55	110	48.44	5.76	45.80	4.27	2.05	0.52	3.54	4.45
55.5	111	32.35	8.48	59.17	5.00	2.07	-0.02	2.91	3.46

Real Depth (cm)	Sample Number	% Sand	% Clay	% Silt	Moment Mean Grain Size (Ø)	Moment Standard Deviation for Mean Grain (Ø units)	Moment Skewness	Diameter at 5% (µm)	Diameter at 7% (µm)
56	112	19.14	9.37	71.49	5.47	1.87	-0.35	2.80	3.28
56.5	113	0.13	12.66	87.20	6.40	1.10	0.96	2.40	2.80
57	114	0.14	12.93	86.94	6.35	1.13	0.99	2.37	2.76
57.5	115	0.50	12.80	86.70	6.30	1.17	0.92	2.37	2.77
58	116	2.51	12.07	85.42	6.23	1.23	0.56	2.47	2.87
58.5	117	58.83	4.59	36.58	3.98	1.99	0.75	4.71	6.16
59	118	30.71	8.40	60.89	5.10	2.04	-0.14	2.90	3.45
59.5	119	17.31	9.79	72.91	5.63	1.82	-0.50	2.72	3.19
60	120	0.05	12.45	87.50	6.36	1.10	1.08	2.44	2.83
60.5	121	0.17	12.07	87.76	6.27	1.15	0.99	2.44	2.85
61	122	0.14	12.42	87.44	6.33	1.12	0.99	2.43	2.82
61.5	123	0.14	12.12	87.74	6.34	1.11	0.96	2.48	2.88
62	124	0.08	13.16	86.76	6.37	1.12	1.05	2.33	2.72
62.5	125	0.10	12.85	87.06	6.37	1.11	1.00	2.41	2.80
63	126	39.76	7.23	53.01	4.59	2.03	0.36	3.14	3.83
63.5	127	0.10	12.35	87.55	6.36	1.10	1.00	2.48	2.87
64	128	0.05	13.09	86.86	6.39	1.09	1.14	2.36	2.75
64.5	129	0.10	13.09	86.81	6.35	1.13	1.03	2.35	2.74
65	130	0.00	15.29	84.71	6.54	1.09	1.17	2.18	2.57
65.5	131	0.00	13.62	86.38	6.44	1.08	1.11	2.35	2.72
66	132	0.06	13.02	86.92	6.39	1.10	1.04	2.39	2.78
66.5	133	0.06	13.52	86.42	6.41	1.11	1.04	2.35	2.73
67	134	0.00	14.25	85.75	6.50	1.07	1.10	2.30	2.68
67.5	135	0.03	13.32	86.65	6.39	1.11	1.06	2.36	2.75
68	136	0.00	14.63	85.37	6.48	1.10	1.10	2.26	2.63
68.5	137	0.00	14.02	85.98	6.48	1.07	1.14	2.34	2.70
69	138	0.04	14.19	85.77	6.48	1.09	1.06	2.30	2.68
69.5	139	0.00	14.39	85.61	6.50	1.07	1.12	2.27	2.64
70	140	0.11	13.84	86.05	6.34	1.18	0.94	2.33	2.70
70.5	141	0.00	14.28	85.72	6.43	1.12	1.10	2.31	2.67
71	142	0.00	15.14	84.86	6.51	1.10	1.14	2.22	2.59
71.5	143	0.06	14.22	85.71	6.49	1.09	1.04	2.31	2.68
72	144	0.00	14.03	85.97	6.46	1.10	1.06	2.35	2.71
72.5	145	0.04	13.92	86.04	6.48	1.08	1.05	2.34	2.71
73	146	0.00	13.88	86.12	6.47	1.08	1.09	2.32	2.70
73.5	147	0.00	15.51	84.49	6.56	1.10	1.11	2.19	2.56
74	148	0.00	14.32	85.68	6.57	1.03	1.22	2.31	2.68

Real Depth (cm)	Sample Number	% Sand	% Clay	% Silt	Moment Mean Grain Size (Ø)	Moment Standard Deviation for Mean Grain (Ø units)	Moment Skewness	Diameter at 5% (µm)	Diameter at 7% (µm)
74.5	149	0.00	14.00	86.00	6.58	1.00	1.28	2.32	2.70
75	150	0.00	13.28	86.72	6.46	1.07	1.12	2.36	2.74
75.5	151	0.00	12.71	87.29	6.43	1.06	1.11	2.42	2.81
76	152	0.00	13.14	86.86	6.46	1.06	1.10	2.37	2.76
76.5	153	0.00	13.86	86.14	6.48	1.09	1.06	2.33	2.70
77	154	0.00	14.89	85.11	6.59	1.04	1.26	2.25	2.61
77.5	155	0.00	14.49	85.51	6.59	1.01	1.30	2.25	2.63
78	156	0.00	14.89	85.11	6.61	1.02	1.33	2.25	2.62
78.5	157	0.00	14.12	85.88	6.55	1.02	1.30	2.28	2.66
79	158	0.00	14.11	85.89	6.51	1.05	1.24	2.26	2.65
79.5	159	0.00	13.95	86.05	6.53	1.02	1.29	2.28	2.67
80	160	0.00	13.13	86.87	6.46	1.03	1.24	2.37	2.76
80.5	161	0.00	13.60	86.40	6.51	1.02	1.23	2.35	2.73

Real Depth (cm)	Sample Number	Diameter at 10% (µm)	Diameter at 16% (µm)	Diameter at 50% (µm)	Diameter at 84% (µm)	Diameter at 90% (µm)	Diameter at 95% (µm)	Diameter at 98% (µm)
0.5	1	4.53	6.75	22.34	185.85	236.59	304.84	383.25
1	2	4.31	6.96	26.98	177.27	229.70	297.97	382.78
1.5	3	3.52	5.12	15.54	76.05	180.05	240.92	302.72
2	4	3.70	5.45	17.77	160.53	217.07	284.22	368.59
2.5	5	3.69	5.47	19.30	196.74	243.18	312.29	390.31
3	6	3.34	4.80	15.24	66.88	180.55	243.58	307.78
3.5	7	3.47	5.10	17.52	172.22	221.93	283.88	353.49
4	8	3.01	4.09	11.61	27.24	34.74	45.18	56.70
4.5	9	3.60	5.32	18.31	170.78	218.74	278.97	350.27
5	10	4.27	6.76	32.49	238.07	286.35	356.83	426.04
5.5	11	3.70	5.99	29.16	221.36	271.36	344.17	415.23
6	12	2.96	4.06	12.01	27.51	34.50	44.57	55.99
6.5	13	4.46	7.12	100.29	269.20	315.51	379.77	448.49
7	14	4.95	7.92	75.93	260.42	307.51	374.18	442.70
7.5	15	3.53	5.01	16.23	206.13	250.44	318.47	392.29
8	16	3.82	5.68	35.17	239.92	286.73	356.29	424.51
8.5	17	4.80	7.81	146.79	280.39	328.31	387.26	455.32
9	18	2.55	3.40	12.60	157.05	193.63	237.20	284.50
9.5	19	3.19	4.78	52.31	238.53	280.17	343.93	402.99
10	20	2.84	4.00	24.94	209.42	248.12	302.42	360.68
10.5	21	2.53	3.40	11.54	165.19	211.66	265.19	326.69
11	22	3.61	5.61	88.15	250.92	294.21	361.56	427.14
11.5	23	3.84	6.17	138.24	272.26	316.94	379.50	447.36
12	24	4.40	7.33	157.09	282.85	330.55	388.11	455.80
12.5	25	4.22	6.68	107.56	266.53	311.56	376.18	444.13
13	26	4.79	8.21	162.72	288.41	337.68	392.88	460.38
13.5	27	4.17	6.74	144.71	272.64	316.61	378.88	446.39
14	28	4.34	7.38	153.98	277.19	322.03	382.03	449.42
14.5	29	3.90	6.25	133.04	256.05	297.32	363.93	428.46
15	30	2.69	3.61	13.55	180.60	219.58	269.54	331.69
15.5	31	3.40	5.27	67.62	238.67	279.11	341.06	398.55
16	32	3.51	5.46	80.51	235.88	275.31	335.82	395.45
16.5	33	3.56	5.38	87.86	243.52	285.80	350.59	411.55
17	34	3.48	5.33	76.60	241.03	282.95	347.22	407.23
17.5	35	4.62	7.87	152.30	265.68	306.53	370.31	434.77
18	36	4.22	6.94	146.54	265.64	308.14	372.07	437.64
18.5	37	3.76	6.08	128.69	252.67	294.07	359.73	422.42
19	38	3.98	6.33	135.87	260.77	303.59	368.21	433.10

Real Depth (cm)	Sample Number	Diameter at 10% (µm)	Diameter at 16% (µm)	Diameter at 50% (µm)	Diameter at 84% (µm)	Diameter at 90% (µm)	Diameter at 95% (µm)	Diameter at 98% (µm)
19.5	39	4.28	6.99	119.20	272.42	319.55	382.46	448.90
20	40	5.53	9.74	170.06	291.44	338.98	394.34	459.78
20.5	41	6.08	11.32	167.14	284.68	331.06	387.09	454.18
21	42	4.76	8.00	150.49	271.84	317.15	377.05	442.41
21.5	43	5.14	8.69	156.58	272.29	315.06	376.32	441.49
22	44	5.20	8.80	140.08	265.55	310.55	369.46	432.61
22.5	45	7.86	17.45	174.53	288.57	335.34	389.67	456.38
23	46	7.96	15.60	184.05	299.42	348.20	399.85	464.88
23.5	47	6.79	12.29	176.03	293.86	342.81	396.39	462.27
24	48	6.46	11.58	181.77	306.12	356.52	408.93	471.05
24.5	49	7.78	14.71	193.37	320.60	367.47	421.47	476.88
25	50	7.34	13.56	184.83	306.19	355.93	407.27	470.10
25.5	51	7.85	14.97	183.53	301.36	349.97	402.23	465.95
26	52	8.41	17.97	179.67	294.94	339.58	395.41	457.84
26.5	53	59.06	95.79	204.17	322.18	367.45	419.11	475.67
27	54	8.28	15.31	181.74	298.36	349.18	399.20	466.15
27.5	55	8.96	17.80	177.13	292.16	340.86	393.47	460.47
28	56	12.00	35.41	195.90	318.80	365.65	418.65	475.55
28.5	57	43.58	86.97	200.63	316.68	362.08	414.13	472.01
29	58	8.36	14.13	201.41	338.72	381.82	437.67	484.24
29.5	59	6.07	9.51	169.49	311.60	361.80	417.20	474.99
30	60	3.69	5.24	15.85	202.41	249.53	314.01	387.28
30.5	61	4.46	6.57	40.96	265.27	315.66	381.08	450.49
31	62	5.66	8.84	162.89	297.94	350.31	403.72	468.68
31.5	63	10.24	22.63	202.30	333.29	377.17	432.30	481.80
32	64	16.00	71.78	214.05	344.77	385.57	440.99	485.72
32.5	65	11.63	34.75	201.93	329.80	374.26	428.79	480.23
33	66	9.70	22.82	196.03	324.37	370.31	424.43	478.21
33.5	67	9.98	21.72	201.25	331.05	375.39	430.30	480.91
34	68	3.98	6.14	38.68	239.90	285.66	354.01	420.57
34.5	69	6.54	10.72	169.75	288.58	336.45	390.77	457.97
35	70	11.98	27.86	191.69	306.68	355.80	405.31	469.25
35.5	71	10.93	23.93	186.33	301.58	352.03	400.92	467.29
36	72	12.38	27.96	192.33	310.35	358.76	409.44	471.29
36.5	73	5.82	9.55	104.00	262.16	308.47	374.26	442.32
37	74	5.11	8.45	55.33	239.61	283.53	350.15	414.06
37.5	75	4.42	7.30	42.07	229.93	274.51	341.88	406.78
38	76	3.23	4.76	17.55	116.29	176.59	230.67	285.39

Real Depth (cm)	Sample Number	Diameter at 10% (µm)	Diameter at 16% (µm)	Diameter at 50% (µm)	Diameter at 84% (µm)	Diameter at 90% (µm)	Diameter at 95% (µm)	Diameter at 98% (µm)
38.5	77	5.24	8.72	129.82	272.26	318.91	381.73	450.34
39	78	4.37	7.11	45.48	237.79	285.40	355.50	424.31
39.5	79	3.32	4.85	18.16	134.12	184.92	236.68	291.87
40	80	3.15	4.48	15.83	122.24	176.66	227.00	278.04
40.5	81	113.89	134.90	208.27	321.85	366.63	417.23	474.77
41	82	3.68	5.23	14.81	77.29	172.65	229.41	285.44
41.5	83	3.87	5.45	14.84	118.31	183.08	236.53	292.00
42	84	3.51	4.81	12.12	26.25	33.96	44.74	56.39
42.5	85	3.32	4.51	11.71	24.80	31.65	41.71	53.23
43	86	3.42	4.71	12.30	26.44	33.31	43.17	54.43
43.5	87	3.25	4.49	12.41	25.96	31.45	38.84	47.25
44	88	3.32	4.56	12.03	24.43	29.72	37.56	46.47
44.5	89	120.19	138.13	206.17	311.93	358.37	406.34	468.85
45	90	120.24	137.75	204.96	309.84	356.77	403.18	467.95
45.5	91	3.45	4.74	12.42	83.85	111.16	141.44	173.00
46	92	3.33	4.49	11.00	20.80	24.82	30.80	37.55
46.5	93	3.27	4.42	11.62	23.43	28.60	36.18	45.18
47	94	3.37	4.58	12.00	24.31	29.53	37.39	46.57
47.5	95	3.41	4.66	12.16	25.42	31.75	40.84	51.03
48	96	5.78	8.59	44.35	267.77	316.17	381.39	450.78
48.5	97	4.40	6.39	19.70	223.80	274.95	348.38	420.16
49	98	6.84	10.34	135.88	312.95	360.64	417.36	474.26
49.5	99	5.10	7.41	40.75	275.48	326.28	388.26	457.12
50	100	5.15	7.51	71.40	243.87	287.27	354.20	418.96
50.5	101	4.64	6.72	22.68	221.88	262.92	325.79	392.98
51	102	4.58	6.63	26.23	222.06	261.31	321.08	388.96
51.5	103	3.94	5.50	15.65	152.64	200.27	249.13	303.61
52	104	4.22	5.95	17.43	175.03	214.33	264.20	327.02
52.5	105	6.11	8.95	124.42	253.90	295.79	360.32	423.21
53	106	6.03	9.10	139.26	262.11	304.80	367.07	430.85
53.5	107	5.54	8.12	75.32	245.42	289.22	355.88	420.02
54	108	6.55	9.67	134.15	257.16	298.73	363.97	427.70
54.5	109	7.82	11.72	152.83	265.72	306.29	369.49	433.75
55	110	5.88	8.73	66.28	231.39	269.25	326.88	389.99
55.5	111	4.36	6.25	18.96	194.35	234.81	291.15	355.65
56	112	4.06	5.64	15.05	135.70	182.47	230.89	280.87
56.5	113	3.35	4.55	11.79	23.71	28.85	36.40	45.34
57	114	3.31	4.52	12.43	25.41	30.60	37.64	46.01

Real Depth (cm)	Sample Number	Diameter at 10% (µm)	Diameter at 16% (µm)	Diameter at 50% (µm)	Diameter at 84% (µm)	Diameter at 90% (µm)	Diameter at 95% (µm)	Diameter at 98% (µm)
57.5	115	3.33	4.59	12.91	27.18	32.93	41.00	50.53
58	116	3.45	4.74	12.60	29.30	38.13	50.98	66.22
58.5	117	8.23	12.99	114.39	292.78	338.96	402.01	460.82
59	118	4.38	6.40	20.37	216.19	270.38	345.79	420.01
59.5	119	3.95	5.52	15.00	131.91	204.43	279.09	368.44
60	120	3.39	4.64	12.52	25.07	29.49	35.30	41.81
60.5	121	3.44	4.81	13.38	27.85	33.13	40.05	47.60
61	122	3.39	4.65	12.67	25.77	30.94	38.09	46.48
61.5	123	3.45	4.71	12.46	25.41	30.63	37.89	46.35
62	124	3.28	4.48	12.28	25.13	29.99	36.33	43.46
62.5	125	3.33	4.52	12.23	24.82	29.62	36.42	44.42
63	126	4.94	7.31	27.60	186.61	216.64	254.54	294.52
63.5	127	3.42	4.64	12.39	24.92	29.66	36.40	44.45
64	128	3.29	4.46	12.22	24.56	28.67	34.02	39.92
64.5	129	3.29	4.47	12.42	26.06	30.80	36.88	43.51
65	130	3.04	4.01	10.78	21.63	25.42	30.25	35.39
65.5	131	3.24	4.32	11.59	23.03	27.17	32.73	38.80
66	132	3.31	4.46	12.00	24.35	28.94	35.10	42.19
66.5	133	3.24	4.35	11.85	24.23	28.73	34.93	41.95
67	134	3.17	4.19	10.91	21.60	25.70	31.35	37.58
67.5	135	3.27	4.40	12.09	24.67	29.01	34.75	41.25
68	136	3.12	4.14	11.18	22.62	26.64	32.00	37.73
68.5	137	3.20	4.23	11.24	22.25	26.08	31.05	36.43
69	138	3.17	4.20	11.15	22.34	26.61	32.84	40.14
69.5	139	3.15	4.18	10.94	21.62	25.51	30.82	36.87
70	140	3.20	4.30	12.50	26.93	31.89	38.53	46.09
70.5	141	3.16	4.21	11.98	24.34	28.16	33.10	38.32
71	142	3.06	4.05	11.07	22.52	26.36	31.11	36.23
71.5	143	3.17	4.20	10.93	21.83	26.29	32.64	40.36
72	144	3.20	4.24	11.36	23.05	27.29	32.92	38.97
72.5	145	3.21	4.25	11.10	22.35	26.69	32.65	39.59
73	146	3.20	4.27	11.26	22.42	26.60	32.29	38.46
73.5	147	3.02	3.98	10.58	21.14	25.08	30.51	36.35
74	148	3.17	4.18	10.44	19.82	23.25	27.95	33.20
74.5	149	3.20	4.22	10.27	19.22	22.47	26.75	31.42
75	150	3.27	4.40	11.40	22.54	26.65	32.18	38.10
75.5	151	3.36	4.54	11.71	23.19	27.40	32.85	38.73
76	152	3.29	4.42	11.28	22.45	26.74	32.40	38.42

Real Depth (cm)	Sample Number	Diameter at 10% (µm)	Diameter at 16% (µm)	Diameter at 50% (µm)	Diameter at 84% (µm)	Diameter at 90% (µm)	Diameter at 95% (µm)	Diameter at 98% (µm)
76.5	153	3.20	4.28	11.18	22.34	26.91	32.91	39.24
77	154	3.10	4.08	10.34	19.81	23.02	27.17	31.78
77.5	155	3.13	4.14	10.27	19.40	22.53	26.55	31.00
78	156	3.10	4.08	10.18	19.19	22.13	25.93	30.03
78.5	157	3.17	4.21	10.67	20.19	23.38	27.32	31.63
79	158	3.16	4.22	11.04	21.67	25.04	29.40	33.88
79.5	159	3.19	4.25	10.81	20.65	23.93	28.15	32.64
80	160	3.29	4.42	11.47	22.31	25.71	29.99	34.36
80.5	161	3.24	4.31	10.93	21.21	24.58	28.84	33.38

VITA

Tyler McNabb

Candidate for the Degree of

Master of Science

Thesis: DEVELOPING PROXIES FOR LATE HOLOCENE SEA-LEVEL AND CLIMATE CHANGE ALONG THE NORTHEASTERN GULF OF MEXICO COAST

Major Field: Geology

Biographical:

Education:

Completed the requirements for the Master of Science in Geology at Oklahoma State University, Stillwater, Oklahoma in December, 2014.

Completed the requirements for the Bachelor of Science in Geology at Florida Atlantic University, Boca Raton, Florida in 2014.

Experience:

Teaching Assistant- August 2014 to December 2014

- Physical Geology Lab

TBC Energy Geologist- May 2014 to August 2014

- Created subsurface maps and cross-sections

Graduate Research Assistant- January 2013 to May 2014

Professional Memberships:

American Association of Petroleum Geologists- July 2011 to Present
Geological Society of America- June 2010 to Present

Abstract:

McNabb, T., Comas, X., and Sumner, D. 2012. Determining Peat Thickness in Subtropical Peatlands using Ground-Penetrating Radar. FAU Undergraduate Research Symposium, April, 6, 2012. Boca Raton, FL